3D crustal structure of the Eastern Alpine region from ambient noise tomography

Irene Molinari, Anne Obermann, Edi Kissling, György Hetényi, Lapo Boschi

Results in Geophysical Sciences 1–4 (2020) 100006

Contents lists available at ScienceDirect

Results in Geophysical Sciences

journal homepage: www.elsevier.com/locate/ringps

3D crustal structure of the Eastern Alpine region from ambient noise tomography

Irene Molinari[a,*], Anne Obermann[b], Edi Kissling[c], György Hetényi[d], Lapo Boschi[a,e,f], the AlpArray-EASI Working Group[1]

[a] Istituto Nazionale di Geofisica e Vulcanologia, Sezione di Bologna, Bologna, Italy
[b] Swiss Seismological Service, ETH Zürich, 8092 Zürich, Switzerland
[c] Institute of Geophysics, Department of Earth Sciences, ETH Zürich, 8092 Zürich, Switzerland
[d] Institute of Earth Sciences, Faculty of Geosciences and Environment, University of Lausanne, 1015 Lausanne, Switzerland
[e] Dipartimento di Geoscienze, Università degli Studi di Padova, Padova, Italy
[f] Institut des Sciences de la Terre de Paris, Sorbonne Université, CNRS, INSU, ISTeP UMR 7193, F-75005 Paris, France

ARTICLE INFO

Keywords:
3D crustal structure
Ambient-noise tomography
Surface wave
Alps
Molasse basin
Moho

ABSTRACT

The tectonic evolution of the European Eastern Alps within the Alpine orogeny is still under debate. Open questions include: the link between surface, crustal and mantle structures; the nature of the Moho gap between the two plates; the relationship between the Alps, the adjacent foreland basin and the Bohemian Massif lithospheric blocks. We collected one year of continuous data recorded by ~250 broadband seismic stations –55 of which installed within the EASI AlpArray complementary experiment– in the Eastern Alpine region. Exploiting surface wave group velocity from seismic ambient noise, we obtained an high-resolution 3D S-wave crustal model of the area.

The Rayleigh-wave group-velocity from 3 s to 35 s are inverted to obtain 2-D group velocity maps with a resolution of ~15 km. From these maps, we determine a set of 1D velocity models via a Neighborhood Algorithm, resulting in a new 3D model of S-wave velocity with associated uncertainties. The vertical parameterization is a 3-layer crust with the velocity properties in each layer described by a gradient. Our final model finds high correlation with specific geological features in the Eastern Alps up to 20 km depth, the deep structure of the Molasse basin and important variations of crustal thickness and velocities as a result of the Alpine orogeny post-collisional evolution. The strength of our new information relies on the absolute S-wave crustal velocity and the velocity gradient unambiguously sampled along the Moho, only limited by the amount and quality distribution of the data available.

1. Introduction

The Alps and their surrounding regions are the results of a complex geodynamic evolution resulting from interactions between the large European plate and the Adriatic microplate. The Alps are characterized by pronounced along-strike changes in structure, which reflect the complex orogenic processes over time. These processes are mainly controlled by the southward subduction of the Alpine Tethys oceanic lithosphere attached to the European plate and the northward migration and anticlockwise rotation of the Adriatic plate (e.g. Serpelloni et al., 2016). Adria is also involved in westward subduction that eventually split into today's rollback subductions beneath Northern Apennines and beneath Calabria (e.g. Faccenna et al., 2001). Main questions though relating to the subduction history, slab rollback (Schlunegger and Kissling, 2015), subduction polarity reversal in Eastern Alps (Lippitsch et al., 2003; Brückl et al., 2007; Handy et al., 2015; Rosenberg et al., 2018) and the evolution and driving mechanisms in the Eastern Alps are still under discussion. The history of large seismic events during the past 1000 years (Hetényi et al., 2018a, their Fig. 1), however, documents continued convergence between the two colliding plates and indicates significant differences in crustal structure and local strain and stress across and along the Alps. Seismic activity at present is pronounced in the Southeastern Alps and their southern foreland (Chiarabba et al., 2005) and also in the northern foreland with a peculiar deep crustal seismicity mainly at the longitudes of Switzerland (Singer et al., 2014).

* Corresponding author.
E-mail address: irene.molinari@ingv.it (I. Molinari).
[1] The complete member list of the AlpArray-EASI Working Group can be found at http://www.alparray.ethz.ch/en/research/complementary-experiments/easi/overview/

https://doi.org/10.1016/j.ringps.2020.100006
Received 17 September 2020; Received in revised form 12 November 2020; Accepted 14 November 2020

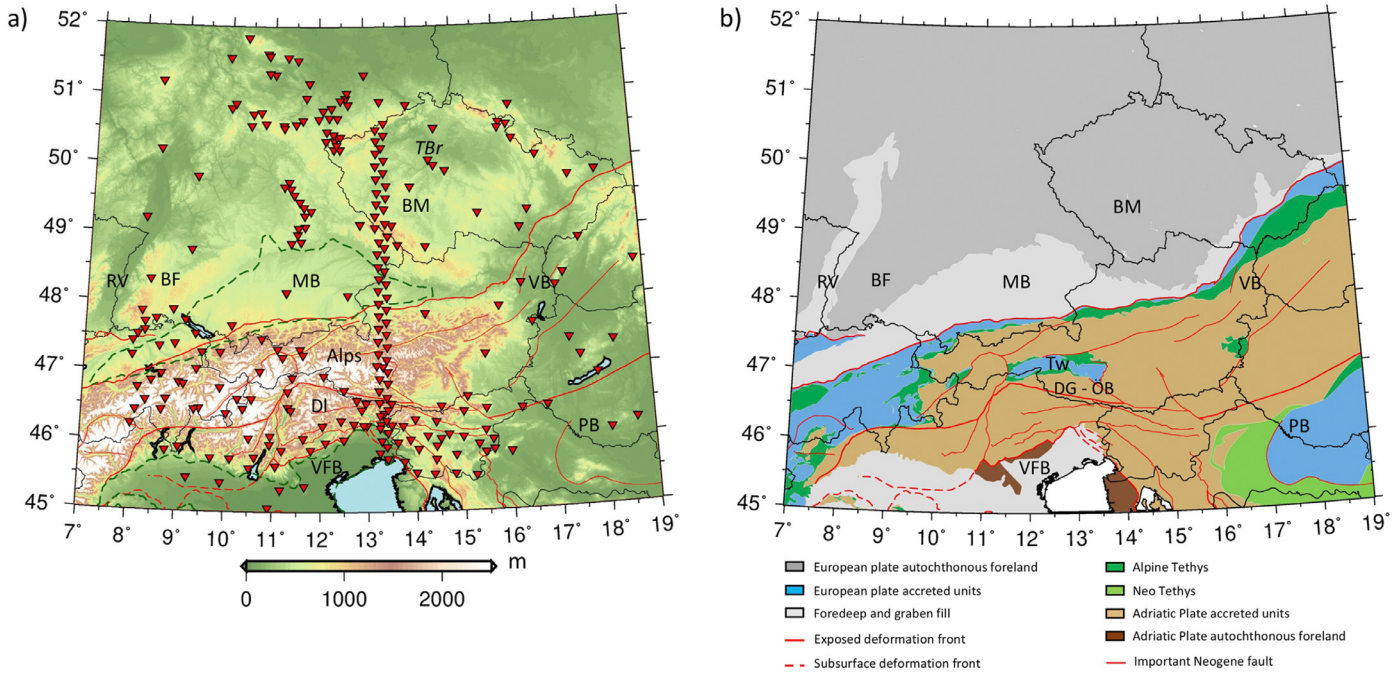

Fig. 1. a) Topography, station distribution (red triangles) and main sedimentary basins in the region: MB=Molasse Basin; RV: Rhine Valley; BF= Black Forest; VFB= Venetian-Friuli Basin; VB= Vienna Basin; PB= Pannonian Basin; BM=Bohemian Massif; Dl=Dolomites; TBr=Teplá-Barrandian region. Dark green dashed lines follow the PP and the MB boundaries at the surface. b) Geological setting of the region where red bold lines represent exposed deformation fronts, red thin lines mark important Neogene faults, while dashed red lins are the subsurface deformation fronts (compilation and simplification after Bigi et al., 1990, Schmid et al., 2004, 2008, Froitzheim et al., 1996, Handy et al., 2010 and Bousquet et al., 2012): Tw= Tauern window, DG – ÖB = Drau-Gurktal and Ötztal-Bundschuh nappe systems.

Within the present day geodynamic system of the Alps and their surroundings, the several relatively small slabs still attached to the European and the Adria plates (Lippitsch et al., 2003; Piromallo and Morelli 2003; Faccenna et al., 2004; Jolivet et al., 2009; Handy et al., 2010; Mitterbauer et al., 2011; Zhao et al., 2016; Kästle et al., 2020), the upper mantle flow around and between these slabs (e.g. Barruol et al., 2004; Faccenna and Becker, 2010; Bianchi et al., 2014; Bockelmann et al., 2013) and the buoyancy of the crustal roots beneath the Alps and the Northern Apennines documented in the Moho maps (Waldhauser et al., 1998; Behm et al., 2007; Di Stefano et al., 2009; Grad et al., 2009; Molinari and Morelli, 2011; Spada et al., 2013) all play major roles as driving forces (e.g., Kissling and Schlunegger, 2018). It is the local crustal structure, however, that links these plate tectonics mechanisms with the locally significantly different seismicity observed all along the orogenic belts in the greater Alpine region (Fig. 1). An up-to-date detailed 3D crustal model, therefore, is of major importance to further improve our understanding of the tectonic evolution of the orogen and of the current seismicity.

The crustal structure of this area has been intensively studied in the past with controlled source seismology experiments: POLONAISE' 97 (Guterch et al., 1999), CELEBRATION 2000 (Guterch et al., 2003; Środa et al., 2006) TRANSALP (Kummerow et al., 2004), BOHEMA III (Karousová et al., 2013) and ALP 2002 (Brückl et al., 2003). These studies significantly contributed to understanding the P and S-wave velocity structure of portions of the Eastern Alps and their connection with the Dinarides, the Bohemian Massif, the Carpathians and the European crust and craton (e.g. Behm et al., 2007; Grad et al., 2009; Sumanovac et al. 2009). In particular, Behm et al. (2007) derived 3D P-velocity model from Pg waves, a Moho map and a Pn-velocity map of the Eastern Alps, while Behm (2009) provided a 3D S-model based on refractions from within the crust (Sg phases), and a Moho map modelled by reflections (SmS) from the Moho discontinuity.

Moving to the Bohemian Massif, Hrubcová and Środa (2008) used refraction and wide-angle reflection data along the CEL10 and ALP04 profiles to derive 2D P-velocity models crossing the region while Hrubcová and Geissler (2009), integrating the receiver functions and refraction and wide-angle reflection modelling, investigated the Moho depth and the crustal structure in the Vogtland/West Bohemian region. Karousová et al. (2012) compiled a 3D P-model of the Bohemian crust integrating the results of the seismic profiles collected during the various active experiments mentioned above, and Karousová et al. (2013) imaged the underling upper mantle via high resolution body wave tomography.

Passive seismological methods also contributed to image crustal thickness, primarily through P-to-S converted waves (receiver functions), revealing intra-crustal structures and indicators of anisotropy (e.g. Kummerow et al., 2004; Wilde-Piórko et al., 2005; Geissler et al., 2012; Bianchi and Bokelmann, 2014; Bianchi et al., 2015; Hetényi et al., 2018b, Stipčević et al., 2020). These studies, based on permanent and temporary station data and primarily with imaging results in 1D and 2D, have revealed the root of the Eastern Alps beneath the orogen with significant spatial variability, parts of major thrust faults going under the mountain belt, locally the Conrad discontinuity, basins adjacent to the Alps, and the structure beneath the Bohemian Massif.

Body wave tomography studies of the crust exist, the majority of them though regarding P wave velocity only and often their spatial extent is limited to portion of the Alpine region (e.g. Michelini et al., 1998; Diehl et al., 2009; Anselmi et al., 2011; Bressan et al., 2012; Viganò et al., 2015) or to the Italian peninsula (Di Stefano et al., 2009; Gualtieri et al., 2014; Di Stefano and Ciaccio, 2014). Ambient noise tomography techniques allow to infer crustal shear velocities (v_S) derived from surface waves extracted from seismic ambient noise. These methods are well suited to image the near-surface 3D S-wave velocity structure at a resolution that only depends on the network configuration, highlighting important features such as basins, upper crustal structures, the crustal thickness. Recently, numerous studies have been published at European scale (e.g. Kästle et al., 2018; Lu et al., 2018, Lu et al., 2020), defining the large-scale structure of the European crust and upper mantle. At a more local scale, Guidarelli et al. (2017) and

Qorbani et al. (2020) imaged the structure of the uppermost 20 km of the Eastern Alps finding a strong correlation with the geology and tectonics of the region.

Studies involving 3D gravity modelling can also provide constraints on the crustal structure as shown by e.g. Spooner et al. (2019), although the spatial resolution of this approach is limited.

Other useful information on crustal structure of the Eastern Alps and surrounding regions, can be found in Spada et al. (2013), who by combining CSS and receiver functions results, derived a consistent Moho map of the Italian peninsula and Alpine arc. Recently, Magrin and Rossi (2020) collected and critically assembled various data from the literature resulting in a 3D model of the northern tip of the Adria microplate following similar methods applied at larger-scale (EuCRUST07, Tesauro et al., 2008; EPcrust, Molinari and Morelli, 2011).

Recently, the greater Alpine region has been the focus of the AlpArray initiative (www.alparray.ethz.ch) with the installation from 2016 to 2019 of a dense backbone network of broadband instruments (Hetényi et al., 2018c; Molinari et al., 2016; Fuchs et al., 2016; Govoni et al., 2017; Vecsey et al., 2017; Graczer et al., 2018), which was anticipated, from 2014 to 2015, by the Eastern Alpine Seismic Investigation (EASI) experiment (AlpArray Seismic Network 2014). EASI focused on the structure of the Eastern Alps and adjacent areas along a north-south transect at ca. 13–13.5°E spanning from the Bohemian Massif to the Adriatic Sea, with a station spacing of 10 km located in a zig-zag pattern along two adjacent lines. Hetényi et al. (2018b) applied the receiver functions method to the EASI data to define the Moho and intra-crustal interfaces along the swath. They found that beneath the Eastern Alps, the shape of the Moho is consistent with bi-vergent orogenic thickening, with a steeper and deeper-reaching Adriatic plate plunging northwards beneath the European plate.

In this work, exploiting the continuous recordings of permanent and EASI temporary stations, we derive a picture of the crust beneath the Eastern Alps and surrounding region. Our Rayleigh-wave ambient noise tomography highlights sedimentary basins, geological and tectonic bodies to a depth of 30–40 km. Our model represents a reliable reference for further studies to come and is an important benchmark to evaluate tomographic imaging improvements when adding more data.

In the following, we first describe the linear tomographic inversion that provides group-velocity maps; we next illustrate the results of the non-linear inversion for v_S and finally, we discuss our results from a geological/geodynamical standpoint, and compare them to results from the studies mentioned above that touch our region of interest.

2. Rayleigh group velocity imaging

2.1. Data processing and measurements

We collected one year of continuous seismic data, from August 2014 to August 2015, recorded by ~200 permanent broadband stations in the region (Fig. 1, red triangles), complemented with 55 temporary stations deployed during the AlpArray-EASI seismic experiment (Fig. 1, orange triangles). The continuous seismic ambient noise records were downloaded from the European Integrated Data Archive (EIDA, www.orfeus-eu.org/data/eida/). We analyzed the continuous noise records from the vertical component and extracted the empirical Green's function following the processing method described in Obermann et al. (2016, 2019). In particular, we applied in this order: instrumental correction; resampling of the data to a sampling frequency of 5 Hz; band-pass filtering between 1 s and 50 s; elimination of 2 h signal segments that show amplitudes greater than ten times the standard deviation of the daily trace; spectral whitening of the amplitude from 1 s to 50 s; one-bit amplitude normalization; elimination of 2 h signal segments that show amplitudes greater than three times the standard deviation of the daily trace (e.g. local earthquakes). We then calculated the cross-correlation between all station pairs for the remaining two-hour segments and stacked them over the 12 months. To increase the signal-to-noise ratio and following Mordret et al. (2015), we averaged positive and negative lag-times of the cross-correlation to enhance the part of the signal that is symmetric. An example of averaged cross-correlations time series between the station CH.BERNI and the other stations are shown in Fig. 2a, where the surface wave dispersive train is well visible.

We analysed the cross-correlations measuring the group-velocity dispersion curves with a frequency-time analysis (e.g. Ritzwoller and Levshin 1998; Yao et al., 2006) from 2 s to 45 s with a sampling interval of 1 s. Group-velocities from inter-station distances smaller than 1.5 wavelengths and SNR< 5 are not considered. We ended up with more than 12′000 measurements for the central periods between 6 and 25 s (Fig. 2c), with a group velocity range from 2.5 to 3.2 km/s (Fig. 2b). We only considered periods with more than 2′000 measurements, from 3 to 35 s, in our further analysis. From the inspection of the ray coverage maps as a function of period (Fig. 3), it is worth to note that there is a decline in signal quality (SNR ratio) when going from West to East, with the EASI line as a rough boundary. The reason is to be found in the lower spatial density and quality of the farther East stations that make the cross-correlations noisy and difficult to measure. However, each pixel in the eastern region of interest is still crossed by > 20 rays, making them usable for our tomography.

2.2. Inversion method

After measuring the dispersion curves between all available station pairs (Fig. 1) and assuming that the remaining effects of nonuniformity in noise source distribution can be neglected (Boschi and Weemstra, 2015), we derived group-velocity maps from 3 s to 35 s, inverting the group-velocity measurements at each period. Following the methods proposed by Boschi and Dziewonski (1999) in the ray-theory approximation, we set up, for each period, a linear system solved with a least-squares inversion via the iterative LSQR algorithm (Paige and Saunders, 1982). We parameterize the region of interest in terms of $0.1^\circ \times 0.1^\circ$ (i.e. about 11 km × 11 km) cells using, as reference values, the group-velocities predicted by the 1D PREM model (Dziewonski and Anderson, 1981) at different periods. To obtain a stable and smooth solution, we regularised the inversion applying a roughness damping value of 0.35, the equivalent of smoothing the solution. This value was chosen after a trial and error procedure testing different regularization parameter values (see Molinari et al., 2015b for more details) until the variance reduction of the data remained relatively high, and after verification with the resolution test (Fig. 3) that there are no features in our maps with wavelengths shorter than the target resolution (40 km). The topography is not considered during the inversion procedure, because the error introduced by this approximation was estimated to be negligible when compared to the group-velocity variation (e.g. Brenguier et al., 2007).

2.3. Resolution

The horizontal resolution of the group-velocity maps can be qualitatively assessed with a synthetic test (Fig. 3, upper row). We select as "input" model a random 2-D map of velocity anomalies (Fig. 3a) with size and distribution statistically similar to typical seismic maps at this scale length (Husen et al., 2009). The anomalies amplitudes range between −10% and 10% with respect to PREM (Dziewonski and Anderson, 1981) and are filtered with a 2-D Fourier transformation to isolate the wavelengths of interest. The resultant anomalies have a spatial extension > 40 km and < 200 km. We also added Gaussian noise to the data (the standard deviation of random noise is the same as that of the data, 0.2 km/s). We solve the problem using the inversion algorithm, regularization scheme and parameters applied to our real data set. We can say that the minimal structural length of a body to be resolved is 50 km × 50 km and, as a general result, we see that structures larger than ~80 km in both directions are sufficiently well resolved if they

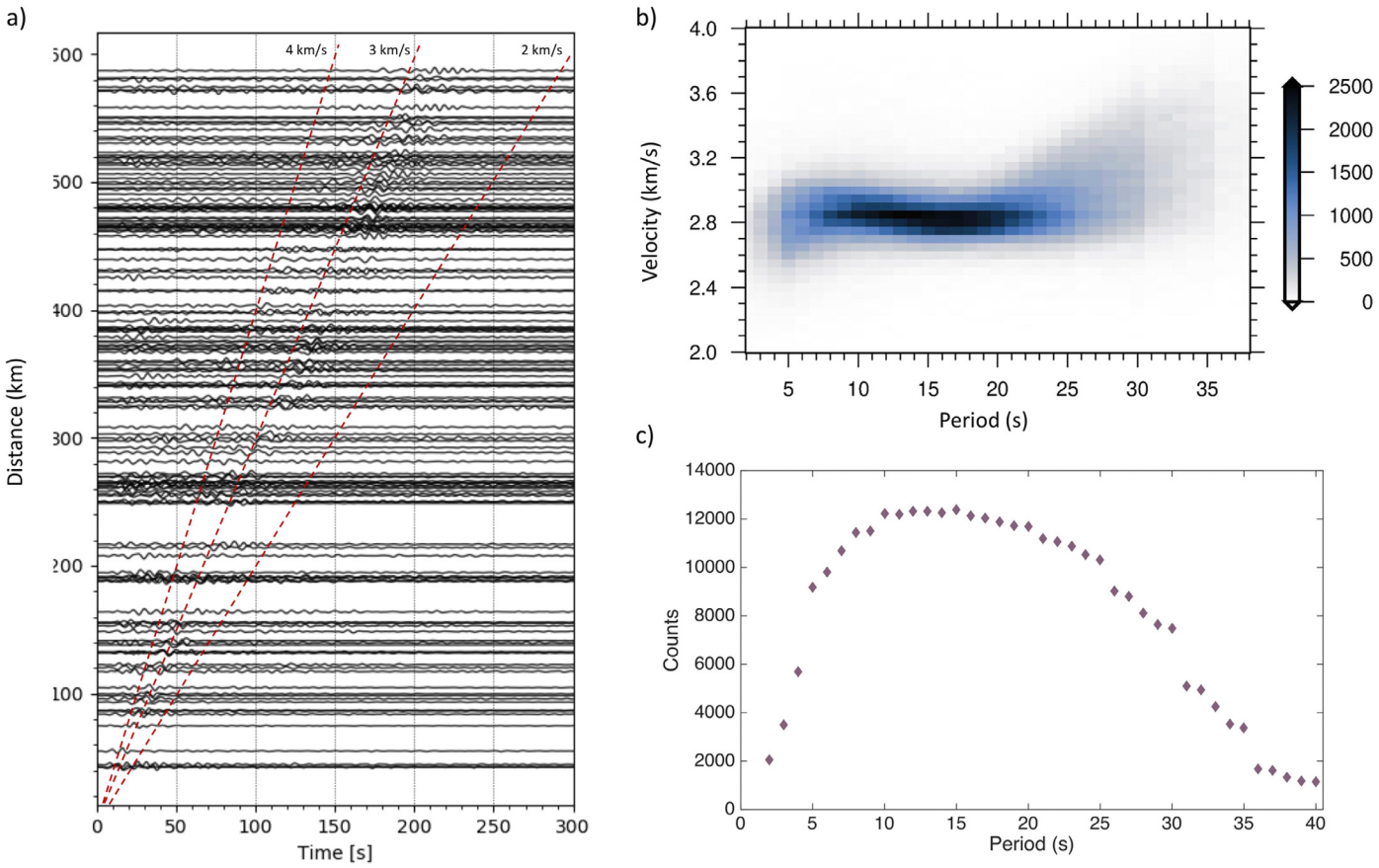

Fig. 2. (a) Example of cross correlations between CH.BERNI station and the other stations used in this study. The dashed lines denote velocities of 4, 3, and 2 km/s.; (b) density plot of the group-velocity dispersion measurements as a function of period; (c) number of measurements for each period.

lay within the region marked by the grey line (Fig. 3b,c,d). For simplicity, based on the test resolution results, we identify two polygons, one for periods within 4-30 s range (Fig. 3b,c) and one for period outside it (Fig. 3d). The crustal structure outside these polygons is poorly resolved because of the ray coverage distribution. We also tested a random model with anomalies of ~30 km to ~90 km wavelength (Fig. S2), but clearly our ray coverage and inversion set-up (mainly our regularization coefficient) is only able to resolve anomalies larger than 40–50 km. The lateral resolution is best for periods from 5 s to 20 s–25 s (in some regions, we are able to resolve structures smaller than 80 km length) and degrades for longer periods. In particular, the Alps and the eastern Germany-western Czech Republic area are better resolved than other regions. While the sign of the anomalies is always reproduced correctly, we note a certain degree of geometrical distortion on the recovered anomalies – for example the two fast (blue) anomalies in central-east Germany (Fig. 3,a,b,c,d green circles). Moreover, the amplitude of the anomalies is slightly reduced, especially for small structures at longer periods (e.g. in eastern Austria, Fig. 3a,b,c,d magenta circles). To gain further understanding of the resolution capabilities of our data set, we calculated the azimuthal coverage of ray crossings following Schaefer et al. (2011). For each cell, we considered the azimuth of the rays crossing within 3.5 km orthogonal distance from the cell center. Then, we split the 180° range of possible azimuths in four slices of 45° and we count the number of rays per slice. We consider a slice well sampled if it is crossed by a minimum of five paths. We classify the directional sampling of a cell as “good”, “fair”, “inadequate”, “poor” when it has four, three, two and one quadrants respectively (Fig. 3, lower row). The outcome of this test is important when interpreting the final 3-D model, the reliability of which is a combination of 2D group-velocity resolution and depth resolution (see Fig. S4).

Between 10 s and 25 s, the ray crossing distributions are very similar and show the best resolution coverage over a large region. The ray crossing at 5 s and 30–35 s periods show that only the area west to the EASI profile, and in particular the Molasse basin and eastern Central Alps are well resolved. Comparing the resolution test results and the cross-firing plots, we deduce that the (relative) amplitude and shapes are well-resolved in such regions dominated by green dots. However, when the geometry of the anomaly is narrow (~40 km), waves with wavelength larger than the average anomaly size, we are not able to resolve it, as documented by the resolution test at 35 s periods. Uniformity in resolution distribution (represented here by ray crossing maps) is of prime importance for reliable results regarding the retrieval of velocity amplitudes and geometries. Moreover, Fig. 3 suggests that in the region filled by uniform green dots for all periods, the 0.1° x 0.1° cell size is appropriate. Some regions though are covered with a mixture between yellow, orange or red dots, suggesting that an increase of the cell size to at least 0.2° x 0.2° in those regions would have been beneficial to obtain more uniform and laterally consistent resolution at depth. However, we decided to use the 0.1°x0.1° degrees working cells, as in this study we aim to reliably resolve the near-surface (top 10–15 km) lateral velocity variations in the whole region by periods up to 20 s (for which we do have a large data set to address the pronounced sedimentary basins around the Alps), the whole crust including the Moho outside of the Alps (where it is in a depth range resolvable by our longest period data), and the regional average crustal velocity variations inside the Alps.

2.4. Group-velocity maps

In Fig. 4 we show the group velocity maps obtained at periods of 5, 10, 15, 20, 30 and 35 s. We only plot cells hit by more than 4 rays and the

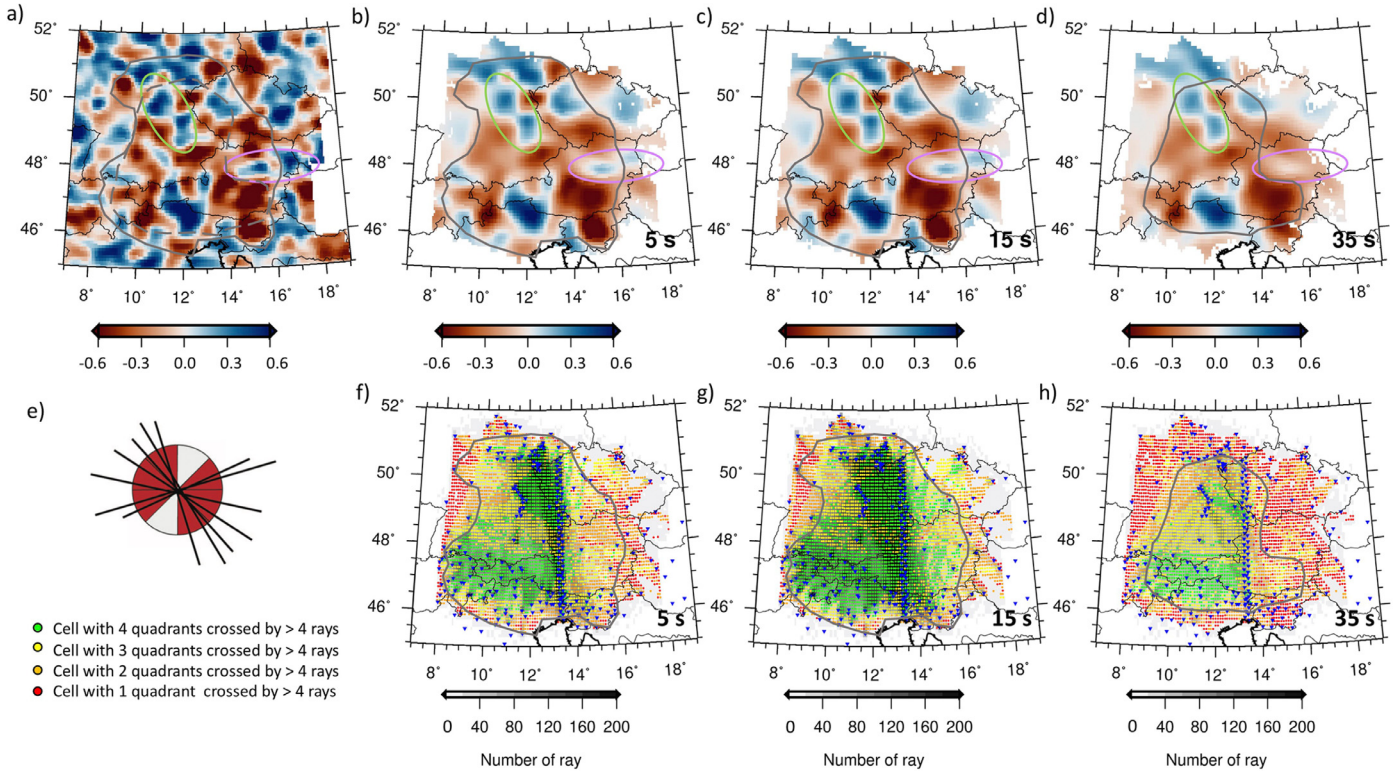

Fig. 3. *(upper row)* Results of the reconstruction test with randomly distributed velocity anomalies with wavelength between 50 km and 200 km as input. a) input models used while b) retrieved models at 5 s periods, c) 15 s and d) 35 s. We highlight the qualitatively well resolved area with the grey lines. The test results for structures within the magenta and green ovals are discussed in the main text. *(lower row)* Combination of ray-crossing and ray-hitting map. At each pixel the total hit count is shown in the background with a grey colour scale and the azimuthal coverage by 4 different colours. (e, modified from Schäfer et al., 2011). A cell is crossed by rays from various directions: we distinguish four quadrants (of 45) within the 180 range of possible azimuths and classify the directional sampling as "very good" when four quadrants are covered by at least five rays each (green dot), "fairly good" when three quadrants are crossed by at least five rays each (yellow dot), "inadequate" when two quadrants are crossed by at least five rays each (orange dot), "poor" otherwise (red dot). Maps at f) 5 s periods, g) 15 s and h) 35 s.

contour line to highlight the well resolved areas. As the period increases, the depth of the group-velocity sensitivity peak increases (Fig. S4). At short periods up to 15 s, our velocity maps are dominated by the effects of heterogeneities within the upper crust. The map at 35 s is sensitive to the Moho outside the Alps but, within the orogen where the Moho is expected to be at around 50 km depth or more, we lack the resolution on this discontinuity. As a general consideration, the group-velocities increase with periods from an average of 2.7 km/s at 5 s to 3.3 km/s at 35 s in agreement with our dispersion measurements (Fig. 2).

At short periods (3–15 s), we expect the shape of velocity anomalies to reflect the main surface geology features present in the region. At 5 s (Fig. 4a), we clearly distinguish the main sedimentary basins as low velocity anomalies. The northern foredeep Molasse basin (MB) exhibits an elongated shape along the northern front of the Alps with an average group-velocity of 2.2–2.3 km/s. The basin is narrow and deep in its western part in Switzerland and widens significantly toward East in Bavaria, where we note a deep basin in the southern half and a shallow basin in the North (i.e. Baran et al., 2014 and references therein). The peak of low velocity is found in south-east Germany, where the basin has its maximum of sediment thickness (Hinsch, 2013; Ortner et al., 2015). The Molasse anomaly, and to a lesser degree, also the Vienna basin anomaly persist, although with higher velocities, at 10, 15 and 20 s suggesting that the depth of these sedimentary basins affects the dispersion curves at periods normally sensitive to the middle to lower crustal structure. It is interesting to note that the low-velocity anomaly crosses the surface boundary of the basin (green dashed line in Fig. 4) indicating that the Molasse basin sediments are underthrusted beneath the Alpine chain (Sommaruga et al., 2012; Hinsch, 2013; Ortner et al., 2015). West of longitude 13°E this feature coincides with the so-called "subalpine Molasse" corresponding to the northernmost and deepest tectonic unit of the Alpine nappe system. It consists of the clastic sediments of Oligocene to Miocene, which were deposited in the southern part of the Molasse Basin and, after the Late Miocene, were progressively incorporated into the thrust belt (Müller et al., 1988). In the easternmost part of the basin, the northern front of the calcareous Alps overthrusted the deepest portion of the Molasse basin by a few km, as documented by drill hole and reflection seismic (Hinsch, 2013).

To the south of the Alps, we distinguish the northern part of the Venetian-Friuli basin (Molinari et al., 2015b) with an average velocity of 2.3 km/s at 5 s and the Ljubljana basin (velocity of 2.4 km/s), which is visible until 7 s period (Fig. S3). At the easternmost part of our domain, where our resolution decreases, we note a low velocity zone until 20 s period which is interpreted as the footprint of the Pannonian basin (e.g., Brückl et al., 2010; Ren et al., 2013). Likewise, at the northeastern termination of the Alps, we observe the trace of the Vienna basin (Behm 2009; Schippkus et al., 2018).

At these 10–20 s periods, high velocity anomalies are mainly related to the Alpine orogenic belt and to the Bohemian Massif. The southern core region of the Eastern Alps, with their crystalline and metamorphic upper crustal basement units, is characterized by average group-velocities of 3.0–3.2 km/s and their shape is well discernible in the maps. Relatively higher velocity areas, at 10 s period, are found in correspondence with the Upper Austroalpine basement and cover nappes (AAN, Fig. 4b), in particular, the Drau-Gurktal and the Ötztal-Bundschuh nappe systems (Schmid et al., 2013). Interestingly, these relatively higher velocities at periods of 10 s and 15 s are confined to the Rieserferner and Drau-Möll blocks south (Scharf et al., 2013) and the Bundschuh block east of the Tauern window units (Rosenberg et al.,

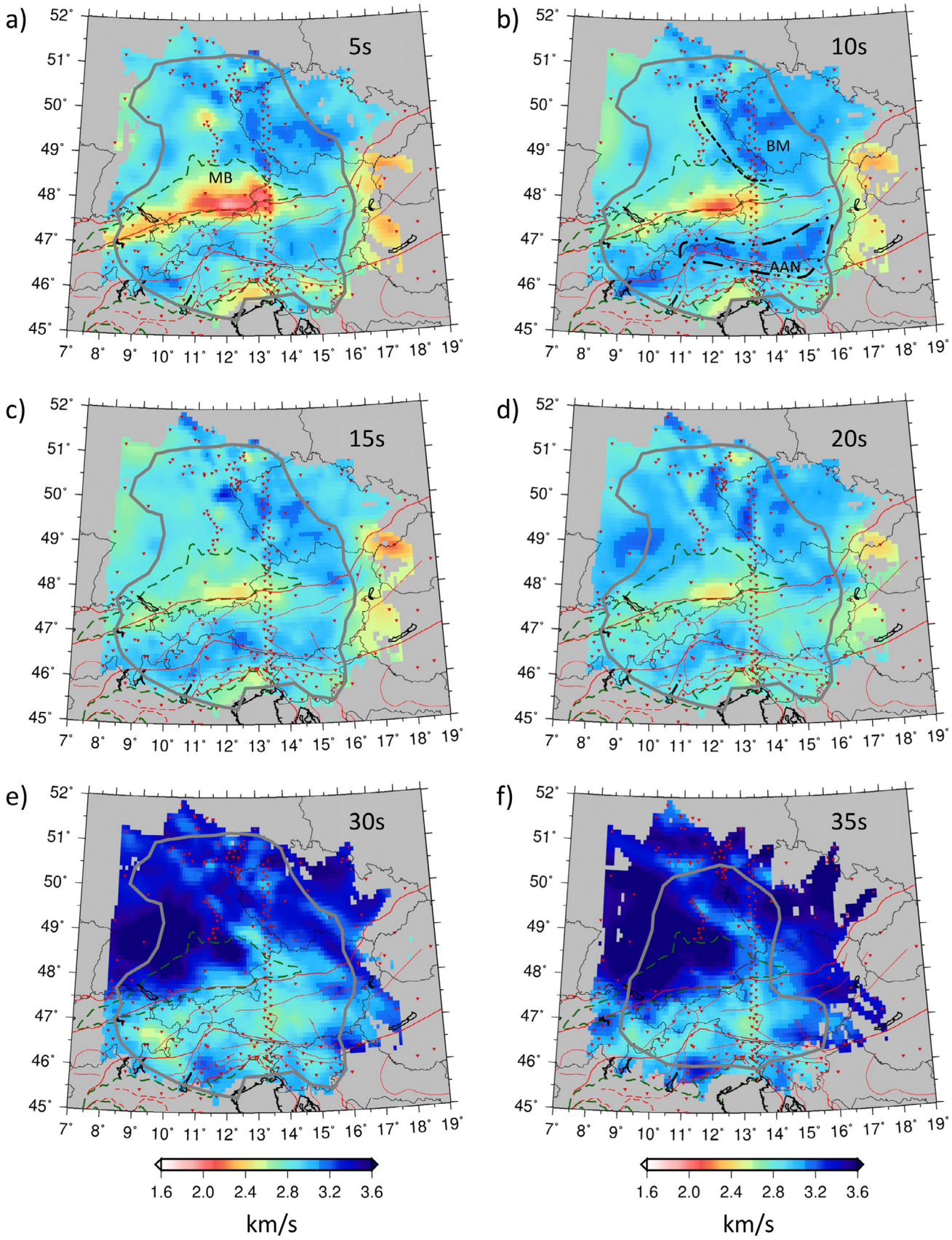

Fig. 4. Group velocity maps as a result of tomographic inversion of ambient-noise dispersion data. Period (s) grows from left to right. The shortest periods samples, e.g., the shallow crustal structure, while the longest ones are sensitive to the crust down to the Moho and below. The dark-green dashed lines represent the surface extension of the Po basin and the Molasse basin (MB), while the red lines are described in Fig. 1.

Table 1
Setting of the variability range of the parameters in the inversion, either in absolute sense, or with respect to the a-priori information (in percent). The a-priori crustal thickness is from Molinari and Morelli (2011) while the mantle model is from PREM (Dziewonski and Anderson, 1981).

	Thickness	v_S (km/s)	v_P (km/s)	Density (g/cm^3)
Uppermost layer	0.5 – 9 km	1.6 – 3.5	2.5 – 5.8	2.65
Upper crystalline crust	20%	2.6 – 4.0	5.6 – 6.5	2.75
Lower crust	20%	3.2 – 4.1	6.2 – 7.0	2.85
Mantle	20 km ±10%	10%	Fixed	Fixed
Mantle	20 km	2%	Fixed	Fixed

2018) that show average velocities of about 2.7 km/s similar to the northern Autroalpine nappes (Fig. 4). In the Bohemian Massif, the group velocity is about 3.1–3.2 km/s at periods from 5 to 20 s, correlated with the well-known presence of metamorphic rocks, granitoid intrusions and volcano-sedimentary rocks in the upper and middle crust (e.g. Hrubcová et al., 2005, 2010).

In southern and central Germany, the group-velocity is uniformly about 2.8–2.9 km/s until periods of 20 s, highlighting the presence of an almost uniform European upper-middle crust (Ye et al., 1995, their Fig. 12).

The shapes and the relative amplitudes of the main features interpreted in this study compare well with anomalies visible in 4s-8 s phase-velocity maps presented by Kästle et al. (2018) and in the 8 s group-velocity map by Lu et al. (2018). Though these studies did not present an interpretation of these specific features, the good correlation of the S-wave anomalies makes us confident about the reliability of our results.

At longer periods (20 s-35 s), the group-velocity is mainly sensitive to the variation of the lower crust, Moho depth and uppermost mantle structure at different locations. This is evident in the contrast between low-velocity Alpine crustal roots (2.8–3.0 km/s) with the high-velocity area (3.9–4.1 km/s) in the northern foreland where 30–35 s surface waves sample the uppermost mantle (Fig. 4). According to, e.g., Brückl et al. (2007) and Spada et al. (2013), the Moho depth in the Eastern Alps reaches down to ~50 km and, in the Central Alps, down to 60 km, while the crustal thickness in the northern Alpine foreland varies between 25 km in the Southern Rhine graben and 35 km in the Bohemian Massif. Relatively high velocities are also found beneath the Dolomites (3.4 km/s) and in the Bohemian Massif (3.7–3.8 km/s), highlighting a non-negligible lateral variation in velocity in the lowermost crust and likely also in the uppermost mantle.

3. S-wave velocity structure

At each cell of our 2D dispersion maps, we build dispersion curves from 3 s to 35 s that serve as input to invert for the local 1D crustal structure. We applied a direct search stochastic method, the "Neighbourhood Algorithm" (Sambridge, 1999a; Wathelet, 2008) to determine isotropic v_S, v_P and layer thicknesses. The method is now commonly used for the depth inversion of dispersion curves (e.g. Molinari et al., 2015b, Kästle et al., 2018) and has the main advantage to deal with the inherent nonlinearity of the problem, exploring the admissible solution space without anchoring the solution to the reference model as a linearized inversion does. The solution space is sequentially and non-uniformly sampled, considering the data fit stored from previous sample runs in the L2-norm, calculated as the difference between observed and modelled dispersion curves.

As in Molinari et al. (2015b), in each 1D cell, we adopt a vertical parameterization defined by 3 crustal layers: a top layer, which can be either sediment or uppermost crustal basement material, a middle layer corresponding to the crystalline upper and middle crust, and a lower layer equivalent to the lower crust. Beneath the crust, we defined 2 mantle layers with a thickness of 20 km each. Wave velocities in each layer are described with a linear gradient, obtained by subdividing each layer into five sublayers.

It is well known that surface-waves lack the sensitivity to image the depth of seismic interfaces (with first-order velocity discontinuities). Therefore, we pre-define the range of acceptable values for all parameters we invert for (Wathelet, 2008) on the basis of a priori information from independent geophysical and geological data. It is worth to recall that, according to Wathelet (2008) the v_S and v_P are directly related through the Poisson's ratio which, in our parameter search, ranges from 0.2 to 0.5. Unlike Molinari et al. (2015b), we did not impose any strong a priori information on the thickness of the known sedimentary basins (e.g. Molasse basin). We did, however, restrict the range of the crustal thickness according to the Moho depth of Spada et al. (2013) where available, and EPcrust (Molinari and Morelli, 2011) elsewhere. Velocities in the mantle layers are taken from PREM model (Dziewonski and Anderson, 1981). In Table 1, we report the variability range of each parameter in the inversion.

We run our algorithm once for each of the 0.1° × 0.1°-size pixels (cells) of our dispersion maps. In total 34,000 possible solution models are evaluated at each 1D cell and the 500 best-fitting models are kept to calculate a mean model for each cell location (preferred model). The root mean square (RMS) of the misfit is shown, as a function of period, in Fig. 5a over all the cells. The misfit is higher at periods longer than 25 s because of the poorer ray coverage. We also show the geographical distribution of the model misfit (Fig. 5b). Apart of the large misfits in the northern part of our region of interest which results from the poor fit at long periods, we do not note a strong geographic dependency of the misfit distribution. The overall misfit depends on whether a good fit is achieved at the shortest periods, where poor estimates of the parameters in the top crustal layer and the coarse parameterization can easily deteriorate it, and at the longest periods where the ray coverage is scarcer.

Before discussing our "preferred" model, we briefly analyse here the robustness of the v_S variations, as a function of depth. It is important to remark that the direct search stochastic method applied here generates an ensemble of acceptable models that, with approximation, could represent the posterior probability distribution function (PDF) of the earth structure reflected by the observations. As extensively discussed in Molinari et al. (2015b), the marginal posteriori PSD of v_S at a fixed depth is not far from a Gaussian distribution, hence the standard deviation σ is a convenient way to represent their width. In Fig. 6 we plot the standard deviation of the a-posteriori PDF for the v_S parameter at three fixed depth (3 km, 15 km and 35 km), representing the three crustal layers. Overall, we note that the standard deviation is between 0.1 km/s and 0.35 km/s. However, as expected, σ is higher at shallow depths, where very short period data do not optimally constrain the structure. The North-East part of our region shows, at all depths, a larger σ that could be explained by the resolution analysis and the ray coverage maps. Beneath the Molasse basin, the standard deviation is higher than in other areas, likely due to the presence of sediments that may cause larger spread of velocity values of well-fitting models. We may also have larger misfit when the interface between two layers regards a

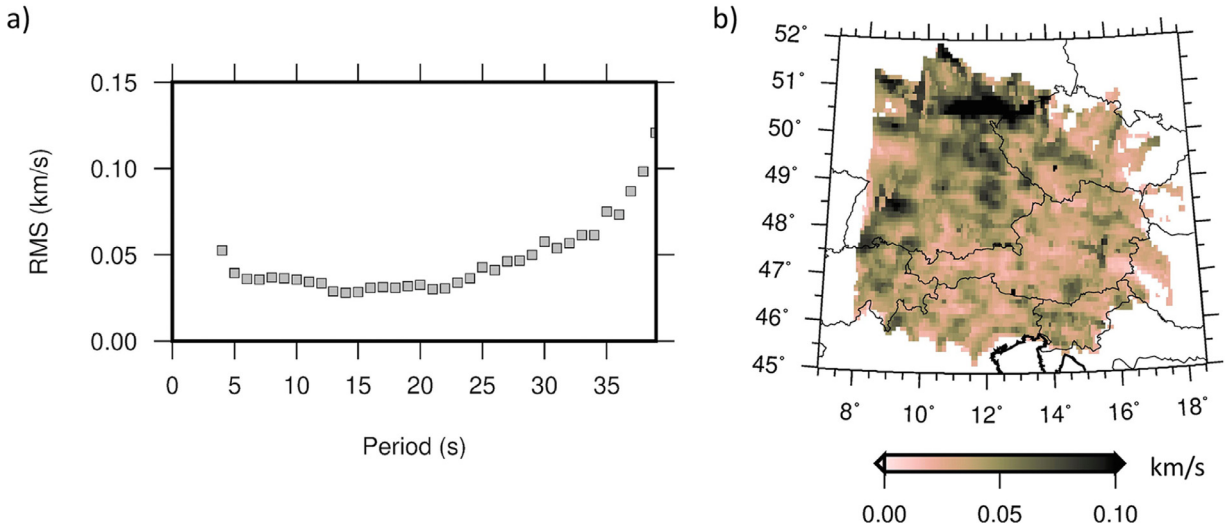

Fig. 5. (a) The root mean square (RMS) in km/s of the misfit between the modelled and measured ambient-noise-group velocity at various periods over all the cells, achieved by the 3D model. (b) Map of the RMS in each cell (over all periods.

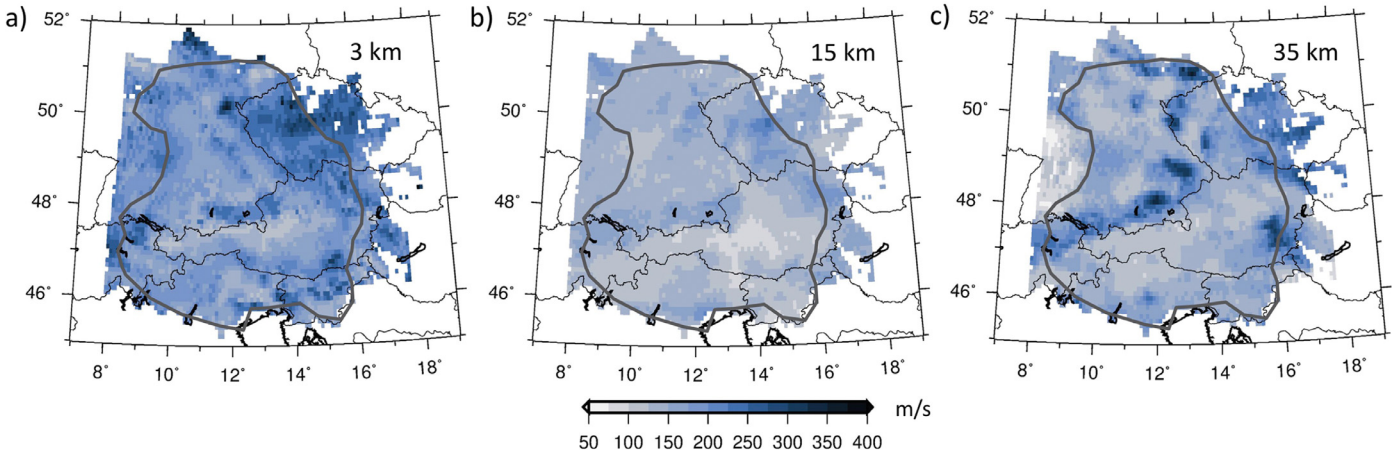

Fig. 6. Maps of the variability range of the v_S parameter in each cell at a fixed depth: (a) 3 km, (b) 15 km, and (c) 35 km depth. It is defined as the standard deviation σ of the Gaussian distribution of the acceptable models (see the main text and Molinari et al. (2015b) for further details).

strong velocity contrast over a short depth range, as likely the case at crust-mantle boundary.

3.1. 1-D local profiles

From the results of applying the above-described inversion scheme, we selected seven 1D profiles from cells that reflect the different geological and structural settings of the study region (Fig. 7). We mark with a grey bar the depth of the Moho according to our a priori model (Spada et al., 2013). The group-velocity data for each cell is generally well reproduced by our model. Unsurprisingly, the fit between observed and reproduced dispersion curves is generally worst for longer periods (>30–35 s) due to the sparsity or lack of good measurements. This leads in some locations, to an unresolvable Moho depth. Where the similarity between best (red) and mean (blue) models is very high, we assume that the solution is generally robust.The introduction of a priori constraints in our inversion scheme (e.g. the Moho depth from Spada et al., 2013), allows us to not bias our final cell models with unrealistic solutions. The shaded regions in the v_S profiles indicate those parts of the cell models that are poorly resolved by our data and that should not be considered for interpretation.

The 1D profile Fig. 7A is representative of the European lithosphere outside the orogenic belts and in the presence of large sedimentary basins. Here, we find a thin sediment layer (velocity ~2.0 km/s and thickness <1 km) under which resides an upper crust with v_S of about 3.2–3.3 km/s until 12 km depth and a relatively uniform middle and lower crust with v_S of 3.6–3.7 km/s. The crustal thickness is about 28 km and we find acceptable models for a Moho depth between 25 and 30 km. This S-wave crustal model corresponds well to the P-wave crustal model derived with CSS methods (e.g., Ye et al., 1995).

Profile B and C (Figs. 6b,c) are samples of the southern border of the Molasse basin and the low short-period group-velocities (< 2.3 km/s) are a clear indication of the presence of a deep basin. In the westernmost location (depth profile B) we obtain a crustal thickness of about 35 km (+/- 3 km) with a top 2 km low shear-velocity layer (1.8 km/s) followed by an upper and lower crust with a gentle velocity gradient similar to the depth-profile at location A. Profile C is located in the deeper part of the Molasse with ~7 km of total sediment thickness and an average v_S of 2.4 km/s. Between 25 and 32 km depth, we note a jump in the velocity, which is interpretable as the Moho discontinuity, comparable with the values found by Spada et al. (2013). Especially for the location B, a broad range of plausible solutions for the top layer suggests that the sediment thickness remains poorly constrained in this location and this sedimentary layer could be, on average, thicker with higher velocity. This trade-off between layer thickness and velocity is typical of surface wave resolution capability and should always be kept in mind.

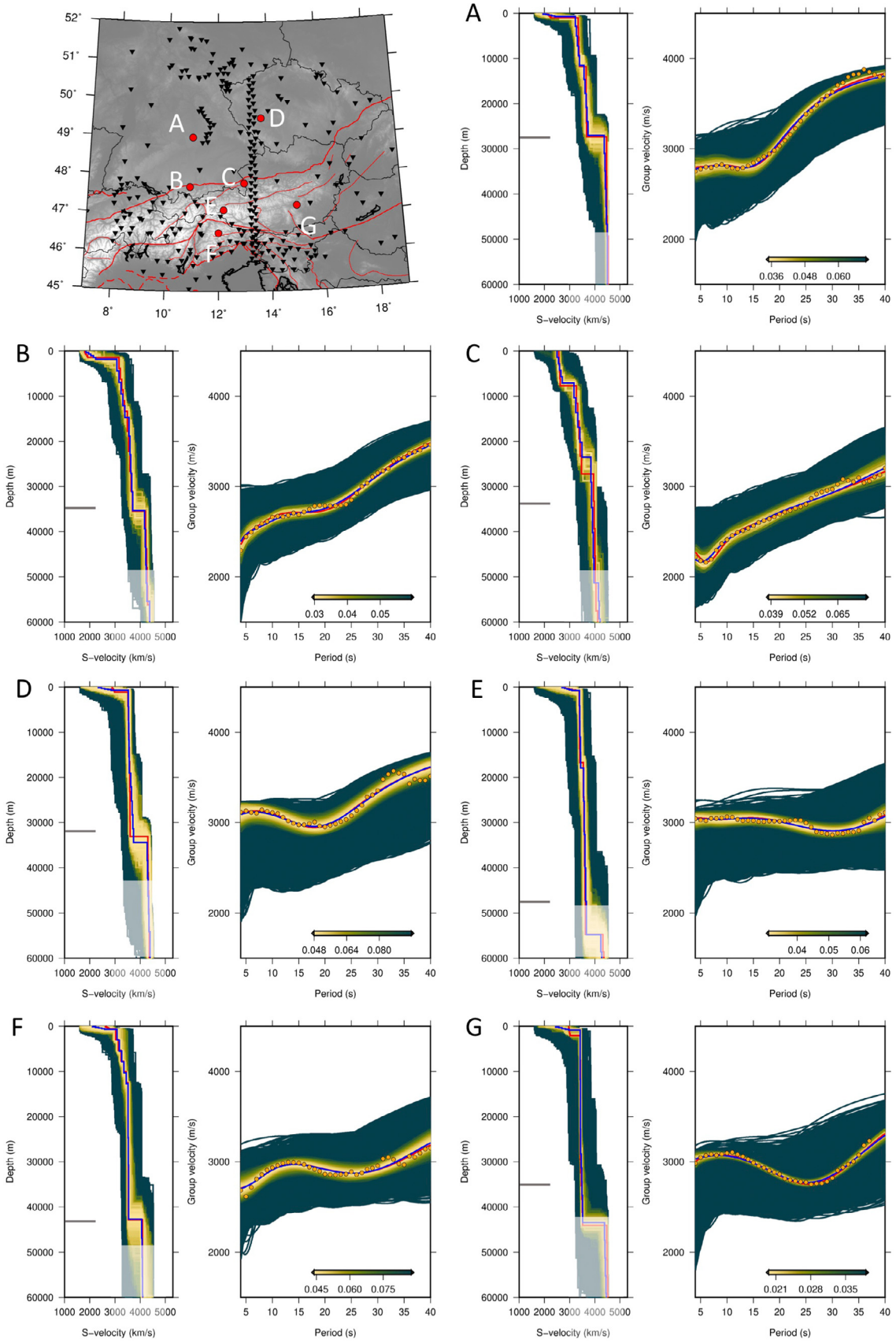

Fig. 7. *1*-D profiles of the v_S resulting from inversion of dispersion curves. In each main plot, we show the suite of resulting v_S profiles, as a function of depth, and corresponding Rayleigh phase and group dispersion curves, as a function of period. Colour of the curves vary depending on the data misfit. The red line represents the best model, while blue line is the preferred model (average of best 500 models). The shaded regions in the v_S profiles indicate poorly resolved parts that should not be considered for interpretation. Grey horizontal lines, where present, indicate the Moho depth from the model of Spada et al. (2013). Orange circles represent the dispersion data to be fitted.

Profile D within (Fig. 7d) the Bohemian Massif, is mainly characterized by a uniform high-velocity crust (v_S ~ 3.5–3.6 km/s) and thickness of about 32 km (±5 km). However, it is clear that the range of plausible models (yellow lines) indicate the presence of a higher-velocity lower-crust in a range between 3.5 and 3.9 km/s. This correlates well with the CEL09 (Hrubcova et al., 2005) refraction seismic transect results, which found a v_P of 6.0–6.2 km/s in the upper crust and 6.7–6.9 km/s in the lower crust. The ALP01 (Brückl et al., 2007) seismic transect found similar v_P in the upper crust but lower velocities in the lower crust (6.5 km/s).

Moving into the Alps (depth profiles at locations E, F and G), we note that the dispersion curves have different shapes in the three locations that result from the complex 3D structure of this mountain chain. They share a relatively low group velocity of about 3.1 km/s for periods of 35 s. This documents that in none of these three locations the longest period surface wave data sampled the uppermost mantle (> 3.1 km/s). The profile E (Fig. 7e) in the Tauern Window is characterized by a uniform crustal structure with shear-velocity of about 3.4 km/s; the Moho depth is not resolvable and should be found at a depth of about 52 km (Waldhauser et al., 1998; Spada et al., 2013).

In the profile location F in the Southern Alps, our inversion results show a strong gradient in the upper crust up to 13 km depth, with velocities between 3.0 km/s at 1 km depth and 3.5 km/s at 13 km depth, correlating with the Mesozoic carbonates at the surface (Dolomites of the Southern Alps). Similar velocities are found also in Qorbani et al. (2020). The lower crust is rather uniform with v_S of about 3.5 km/s. The preferred Moho depth is ~43 km, in agreement with the model of Spada et al. (2013); but again, the Moho is poorly resolved since no clear evidence of mantle velocities is contained in the data.

Profile G is located at the South-East border of the Eastern Alps, a region where our resolution and the ray crossing coverage at periods > 20 s is quite poor (Fig. 3). Here, we do not expect to have enough resolution power to image the lowermost crust and the Moho that according to P-wave velocity evidence should lay between 34 km (Spada et al., 2013) and 42 km depth (Brückl et al., 2007). The crustal structure appears to have a rather uniform velocity profile with v_S of ~ 3.4–3.5 km/s.

3.2. Determination of Moho depth

From Fig. 7, we note that a pronounced Moho velocity interface is obtained when the group velocity at 40 s period is higher than 3.4 km/s, while the result is either no first-order velocity interface at all at the crust-mantle boundary (cell E), or a wide depth range with a velocity gradient and a very weak velocity jump at the interface (cell C) when it is less than 3.4 km/s. The characteristic shape of the dispersion curves in relation to the model parameters has already been noted by Lebedev et al. (2013, their Fig. 1 and 3). The sensitivity kernels and the surface wave resolution power on the Moho discontinuity are tools to understand this non-linear relation. As stated by Lebedev et al. (2013), data suffer from a trade-off between the determination of the Moho depth and crustal and mantle shear-speeds: a non-uniqueness that translates into uncertainty in the Moho depth assessment. Measuring low group velocities (< 3.4 km/s) at periods > 35 s means that our dispersion curves still sense crustal velocities or are still influenced by lower velocities from above. This is due to the broad depth range of surface-wave depth sensitivity functions (see Fig. S4 and Lebedev et al., 2013). In a 45 km thick crust (Fig. S4), 35 s group velocities have their maximum sensitivity around ~35–40 km depth, with a range of influence between 20 and 60 km depth. As demonstrated by Lebedev et al. (2013), group velocities show a strong sensitivity to the Moho depth, which is a desirable characteristic when a homogeneous and dense ray coverage by a continuous series of long period waves (20 s to 60 s) is available, but could lead to an arbitrary determination of the crustal thickness if it is not the case – as, e.g., in the easternmost parts of our model (see Figs. 3h and 6G). To reduce this non-uniqueness, it is recommendable to introduce as much a priori information as possible or to perform a joint inversion with other independent observables. In this work, we let the crustal thickness vary by ~20% from the a priori data, which is a quite considerable variation. However, we note that in those regions, where our data coverage (at all periods) allows a good resolution (i.e. to the West of EASI profile, green dots in Fig. 3) our final model Moho depth agrees very well with the a priori Moho – which was derived from a different seismic method, sensitive to velocity discontinuity interfaces. This is not obvious, as the method of ambient noise tomographic inversion for v_S is rather insensitive to first-order discontinuities. For these reasons, we maintain the model parameter variability range as set in Table 1 and homogeneous for the whole region.

We also note that when a sharp Moho discontinuity is present, the mantle velocity is > 4.1 km/s and the crust is at v_S < 3.9 km/s. We select the velocity iso-contour of 4.1 km/s shown later in Fig. 8 to discuss the discontinuity between the crust and the mantle.

3.3. Discussion of the 3-D shear velocity model

The maps of the v_S structure associated with our preferred model are shown in Fig. 8. At each depth (5 km, 8 km, 12 km, 18 km, 27 km, 40 km), the solution is shown for those cells hit by at least 4 ray paths (at 16 s period). From Fig. 7, we note a number of features that match with surface geology and large-scale tectonic structures. Well-known sedimentary basins and reasonable crustal thickness clearly emerge in our final 3D model.

In the following, we discuss and interpret the several interesting features we find, also in relation to results recently published in the literature.

3.3.1. Shallow crustal structure

In the uppermost part of the crust (5 and 8 km depth – Fig. 8a,b), the Rayleigh-wave shear-velocity model shows prominent low-velocity zones: the Molasse Basin (MB), the Venetian-Friuli basin (VFB), the Vienna Basin (VB) and the westernmost part of the Pannonian basin (PB) in the East, and the Ljubljana basin in Slovenia. Focusing on the MB (Fig. 8a), we note that the shape of the anomaly closely follows the topography border of the basin except in the south-eastern part, where it is shifted towards the Alpine chain. The inner structure of the Cenozoic marine and continental clastic sediments of the Molasse basin is also fairly well resolved. Interestingly, we note a clear inner boundary within the MB around longitude 12°E. This is confirmed by the findings by Ortner et al. (2015), and it correlates at depth with the eastern limit of the remaining European slab (Lippitsch et al., 2003) which evolution has been described in Schlunegger and Kissling (2015) to have greatly influenced the shape of the basin to the west of longitude 12°E. Further to the East, the deepest depression of the basin has been preserved as it was 12 million years ago (Hinsch, 2013; Ortner et al., 2015), when the overthrusting by the Northern Calcareous Alps stopped. Here, the basin reaches ~5–7 km depth with an average v_S of 2.4 km/s and has an extension of ~ 200 km in the E-W and of ~50 km in the N-S direction with the southern part having been overthrusted by the Alps. Conversely, in the W, the basin has been inverted (uplifted) under the effect of the slab rollback (Schlunegger and Kissling 2015). Here, in the Swiss Molasse basin, the depocenter appears shallower (4–5 km) and it is narrower than in the East with a significantly higher average v_S of 2.8 km/s.

The relative low velocity anomaly in the Venetian-Friuli basin (Fig. 8) has values of ~ 2.9–3.0 km/s, typical values for carbonates of the Mesozoic limestone. At 5 and 8 km depth, in this part of the Po Plain, we sample the carbonate layer which reaches a depth of ~ 7–9 km; low-velocity sediments (Quaternary and Pliocene sediments) are shallower, with an average depth of 2–3 km (Molinari et al., 2015a).

In the Easternmost region covered by our data, at 5 km depth (Fig. 8), we image the Vienna basin appearing with a v_S of ~ 2.6–2.8 km/s which continue locally until ~12–15 km depth. Though this area is not well resolved by our inversion (Fig. 3 and mask in Fig. 8), this agrees with the results of Schippkus et al. (2018), who find velocities in a range

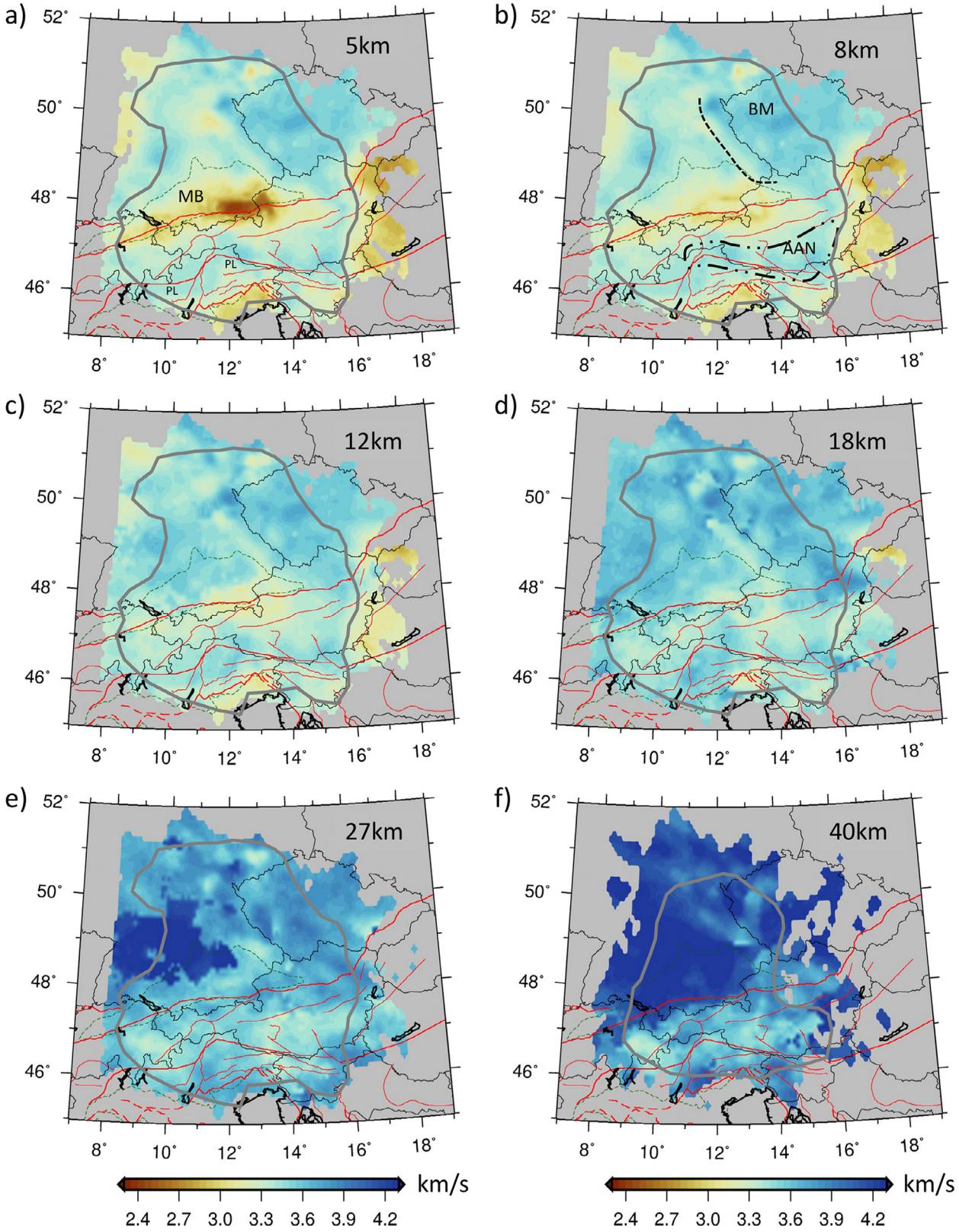

Fig. 8. Shear-wave velocity maps of the 3D model obtained by averaging the 500 best-fit models obtained by the local neighbourhood algorithm inversions. Depth in km is specified on each panel and grows left to right, top to bottom (*a* to *f*). BM=Bohemian Massif; MB=Molasse Basin; AAN=Austro Alpine Nappes; PL=Periadriatic Line. See text for description and interpretation. The dark-green dashed lines represent the surface extension of the Po basin and the Molasse basin (MB), while the red lines are described in Fig. 1.

between 2.3 and 3.0 km/s from 4 to 20 km depth (with greater depth in North-East part of the basin) and with Ren et al. (2013) finding low velocities beneath the Vienna Basin for depths up to ~16 km. We also map the westernmost parts of the Pannonian basin – the Danube basin in the AlCaPa region (Horváth et al., 2006) – with velocities of about 2.9 km/s at 5 km depth, visible until a depth of 8 km. The resolution tests, however, do not allow us interpreting any further the shape and the inner structure of these basins.

Focusing on the fast-anomalies at shallow depth (5–8 km), we clearly distinguish the Bohemian Massif (BM) a mixture of several microplates (Plomerová et al., 2007) amalgamated during the Variscan orogeny (Matte et al., 1990). The high velocity region, with v_S between 3.4 and 3.7 km/s (Fig. 8), appears more as a block, and the relative lateral variation seen in the group-velocity maps (Figs. 4a,b,c,d) is somewhat smoothed in the final 3D model. The general shape of this high-velocity anomaly, however, follows the overall topography documenting that it is a large and stable outcrop of the pre-Permian high-velocity basement now at the surface after erosional processes (Hrubcová et al., 2005). The inner structure of the BM was extensively studied by controlled-source seismology profiles (e.g., CEL09, Hrubcová et al., 2005; SUDETES2003, Hrubcová et al., 2010) with the P-velocities in a range from 6.0 km/s at the top to 6.8–7 km/s in the lower crust. In good agreement with the P-velocity, the highest S-wave velocity anomaly in this study is found in correspondence with the Teplá-Barrandian region.

Another interesting result is the high velocity zone in the Eastern Alps directly north of the Periadriatic line. Here, we mainly see the structure of the shallow overthrusted Austro-Alpine Nappes that, in our model, has a v_S of about 3.4–3.5 km/s at 5–8 km depth. Instead, the Dolomites region shows a lower shear-velocity area (~3.2 km/s) because of its limestone-calcareous rocks. These results are in general agreement with the local ambient noise tomography of Qorbani et al. (2020).

3.3.2. Upper crust

At upper crustal depths (12–18 km, Fig. 8c,d) we note a clear variability in the composition of the crust: a distinct difference between the faster Bohemian Massif and Southern Germany, and the slower region beneath the Alpine chain, Venetian-Friuli basin and Pannonian basin. The shear-velocities in the BM are in a range between 3.5 and 3.8 km/s, typical of granitoids and low- to high-grade metamorphic and plutonic Palaeozoic rocks forming the different BM units (Plomerová et al., 2007 and references therein). It is notable that the structure of the BM does not change much from 5 km to 18 km depth, pointing to sub-vertical boundaries as described in e.g. Mlčoch and Konopásek (2010) and Babuška and Plomerová (2013).

In south-central Germany, v_S is about 3.4–3.6 km/s at 12 and 18 km respectively, as expected for the European crust at the transition between upper and lower crust. Under the Molasse basin, the velocity is ~3.0 km/s, which could partially be a smearing effect of the shallower sediment low-velocity anomaly or could indicate a different composition in the upper crust. In the Pannonian basin, the lower velocities (2.7–2.9 km/s) could be attributed to the locally thick sedimentary rocks in a generally hotter upper crustal environment (e.g. Horváth et al., 2015).

The Central and Eastern Alps are characterized by a quite heterogeneous upper crust. The Southern Alps, bounded by the Periadriatic Line and Southern Alpine thrust (Doglioni and Bosellini 1987), exhibit a relatively high v_S (3.6 km/s), anomaly also present in the body wave tomography results of Diehl et al. (2009) and Di Stefano and Ciaccio (2014). Instead, the Eastern Alps, comprised of Adria-derived units including crystalline basement rocks and thick carbonate cover sequences (Northern Calcareous Alps), show lower velocities of ~3.2–3.3 km/s with a possible increase in the north easternmost parts to 3.6 km/s. More to the West in the Swiss Alps, the shape of the anomalies remains almost constant from 5 to 18 km depth. Here, v_S is in a range between 3.2 and 3.4 km/s corresponding to the values found in the northern foreland for the crystalline upper crust.

3.3.3. Lower crust and Moho depth

Moving from middle to lower crust (27–40 km depth, Figs. 7e,f) we note the high-velocity region in Central-South Germany with typical uppermost mantle values (> 4.1 km/s) indicating that we are sampling the mantle lithosphere. The Moho depth is around 24–28 km, in agreement with previous works (e.g. Spada et al., 2013; Molinari et al., 2015b; Kästle et al., 2018).

The Bohemian Massif shows relatively high lower-crustal shear velocities (3.8–3.9 km/s) in the whole region (Fig. 8e). This correspond, according to the interpretation of CEL09 and CEL10 seismic profiles by Hrubcová and Środa (2008), to high P-velocities in a range between 6.5 and 7.8 km/s. Plomerová et al. (2016) found that the average crustal thickness in the BM is about 33 km and the Moho depth varies between 26 and 40 km on relatively short distances. At 40 km depth (Fig. 8f), we find lower mantle velocities in the Teplá-Barrandian regions, suggesting a shallower Moho depth. However, in this region, the crustal structure is significantly different and more complex than further West, and our results could suffer from resolution problems and/or from inadequate initial reference layering. Consequently, we do not further interpret our results in more detail.

At 27 km depth, the Alpine chain shows middle-lower crustal velocities between 3.4 and 3.7 km/s. In particular, we note a relatively low velocity zone in eastern Switzerland at the borders with Italy and Austria that indicate the presence of deep crustal roots. Here, the Moho depth is particularly well known to be about 55 km (Kissling et al., 2006 and references therein) and this depth is beyond the limit of our depth resolution (see Fig. S4) that is controlled by the maximum period measured in the dispersion curves. In the East, the 27 km depth slice touches the transition zone between the Pannonian Basin and the Eastern Alps (around 16E and 47–48 N) and samples the lowermost crust just above the Moho (Ren et al., 2013; Hetényi et al., 2015) with relatively low velocities of about 3.4–3.6 km/s.

At 40 km depth (Fig. 8f) we mainly sample the upper mantle in the whole region with the exception of the Alps, where we still find relatively lower, crustal velocities.

3.4. 2-D cross-sections

Vertical sections (Fig. 9) of our final 3D model reveal several important tectonic and geological features highlighting the different crustal domains present in the region. They allow some considerations about model reliability. These sections are not smoothed in order to well identify parameterization and thus to avoid over-interpretation of the results. Because of our resolution limit, we must focus on the structure at a depth shallower than 45–50 km to the West of longitude 13°E and on depths <30–40 km East of 13°E. For this reason, most of the deep crustal Alpine structures, in particular the mountain roots, are poorly resolved or remain unresolved and some appear as a broader velocity gradient zone.

To better identify the transition between crust and mantle, we marked the 4.1 km/s v_S iso-contour on these profiles. From the work of Vilhelm et al. (2016), who determined the seismic velocities for the rock outcrop (peridotite), we deduced that a velocity of 4.1 km/s could best represent a volume of mostly, if not all, peridotite (uppermost mantle lithosphere) and thus we consider this isoline as a first-order estimate of the Moho depth. The Moho depth results from Hrubcova and Sroda (2008), Hrubcova and Geissler (2009), Spada et al. (2013), Hetényi et al. (2018b) and Magrin and Rossi (2020) are overlaid to our 2D sections for comparison.

The *Aa* profile (Fig. 9) documents the significant variations in crustal structure and thickness between the "normal" Hercynian European crust (e.g. Blundell et al., 1992) and the Bohemian Massif crust. The first part, until 180 km, shows typical crustal velocities (~3.0 km/s in the upper crust and 3.7 km/s in the lower crust) and a sharp Moho boundary at 25–30 km, with a perfect fit with the Moho by Spada et al. (2013). The north-eastern part has a broader gradient at the crustal-mantle transi-

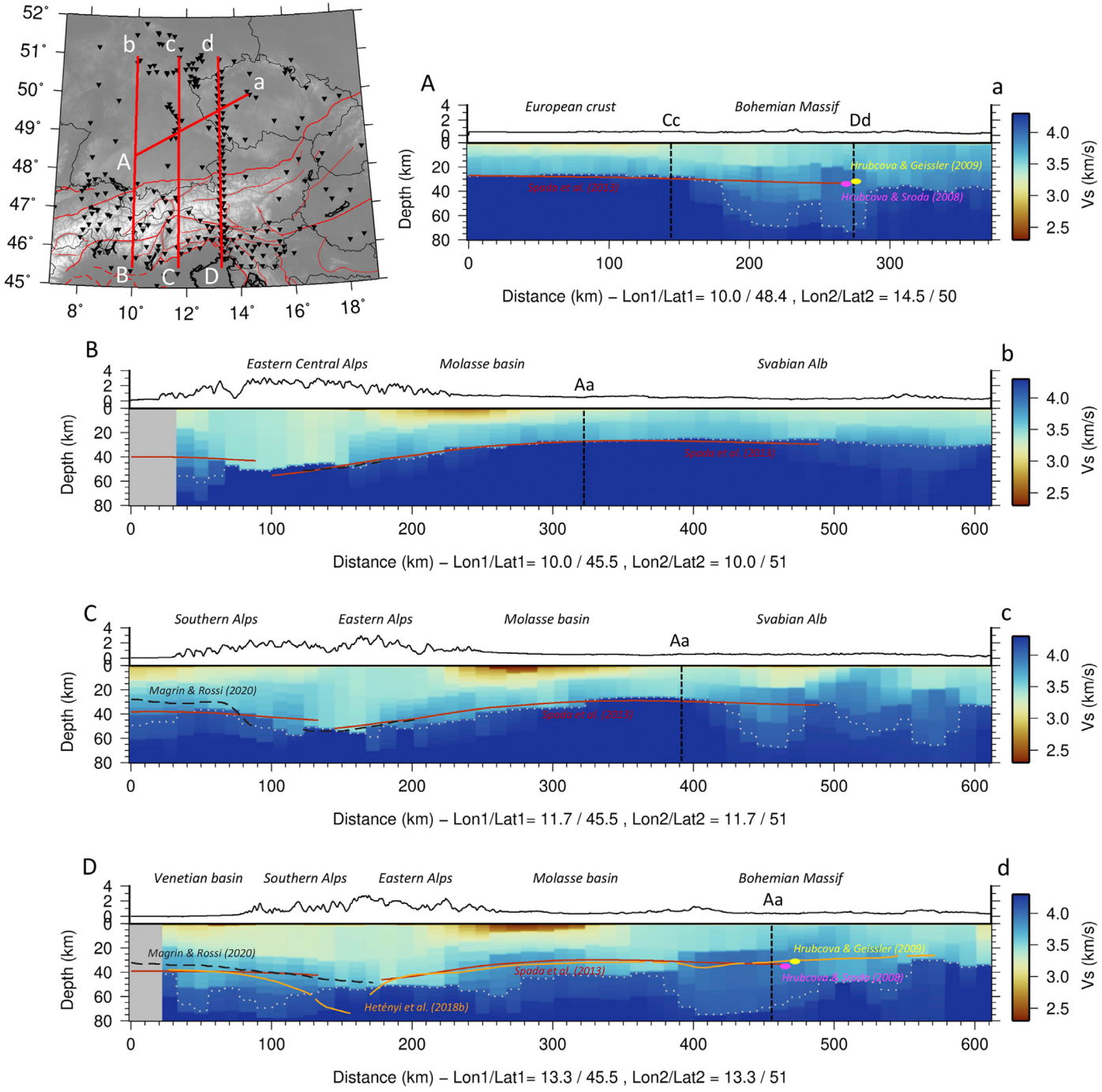

Fig. 9. Vertical sections of the shear velocity model along the profiles shown on the map. The sections are not smoothed in order to well identify the parameterization. In each section the isoline at v_S = 4.1 km/s is highlighted (grey dotted line). The Moho determination from Spada et al. (2013) (darkred line), Magrin and Rossi (2020) (black dashed line), Hetényi et al. (2018b) (orange line), Hrubcova and Geissier (2009) (yellow dot) and Hrubcova and Sroda (2008) (magenta dot) are reported in the figure for comparison.

tion with sensibly higher velocities, likely indicating the different origin of the two crustal domains. In the Bohemian Massif (Fig. 9, profile *Aa*, and the northern part of D*d*), we do not have good resolution on the deep structure and our final 3D model could suffer from wrong initial reference layering. The complex deep crustal structure between the *Cc* and *Dd* crossing points should be fairly well resolved. Hrubcova and Geissler (2009) show how the combination of high-resolution RF and CSS modelling leads to a consistent crustal model in the northwestern part of the BM with a much thinner lowermost crustal layer and a slightly shallower Moho that rests just above the mantle velocity depth found in our model (Fig. 9 *Aa*). Furthermore, along the *Dd* profile, the results by Hrubcova and Geissler (2009) correspond very well with the results originating from Behm et al. (2007), later interpreted and integrated into the Moho map by Spada et al. (2013). Karousová et al. (2012) derived a Moho depth map from a compilation of CSS profiles and, according to this study, the BM Moho depth is increasing, from N to S, from 32 km to 38–40 km and has deepest Moho at about 40 km beneath the southern Moldanubian region. Thus, E and N of the crossing points of Aa with Dd, the estimate of the Moho depth in the BM shows up as a gradient and is systematically deeper in our 3D model than in the models published in the literature.

The *Bb, Cc* and *Dd* profiles in Fig. 9 cross our study region from S to N and show the crustal variability along the longitude axis. In particular, we can easily appreciate the depth and extension of the main sedimentary basins (Molasse basin and Venetian-Friuli basin). Moving towards N, the crust gradually thins reaching 25–30 km beneath the northern foreland. Within the crust, the sediments and upper and lower crustal domains are clearly visible. The Molasse basin is a prominent feature and the sediments overthrusted by the Northern Calcareous Alps are clearly visible. Beneath the Molasse basin, especially in profile *Dd*, the Moho "discontinuity" presents itself as a smooth transition zone that could be a vertical "leaking" effect of the low basin velocities in our non-linear depth inversion. Focusing on the Alpine chain, we found a pretty uniform 25 km thick upper crust in the Eastern Alps with an average v_S of 3.3–3.4 km/s, while the lower crust in some regions exhibits a strong velocity gradient with a high average velocity of about 3.6–3.7 km/s and its thickness decreases from W to E (sections *Cc* and *Dd*). The Southern Alps show a lower velocity in the upper crust than Eastern Alps, with a lower crust characterized by a quite strong velocity gradient. The crustal thickness reaches a maximum at the transition between Southern and Eastern Alps with values of about 55–60 km and thins gradually in the Eastern Alps to 40–45 km. However, as already mentioned, east of the EASI profile, our resolution degrades at ~30 km depth. Recently, Hetényi et al. (2018b) exploited the receiver functions method on the EASI seismic profile proposing an Alpine crustal root of >70 km depth with a broad vertical velocity gradient at the location of the former Moho "gap", while showing outside the Alpine chain a good correlation with the Moho by Bianchi et al. (2015), Spada et al. (2013) and Behm et al. (2007) (section *Dd*).

In the profiles *Bb* and *Cc* (Fig. 9), we see a nearly perfect fit between our Moho and the one obtained by Spada et al. (2013). The correlation though is less good for the profile *Dd,* where we note a systematic tendency to obtain a deeper and laterally more variable ANT-Moho than Spada et al. (2013) and Hetényi et al. (2018b). The Moho depth of Magrin and Rossi (2020) agrees well with Spada et al. (2013) beneath the Eastern Alps but remains somewhat shallower beneath the Southern Alps and the Venetian-Friuli basin. In those regions, where the correlation between the Moho topography models is not very good, we see a more complex velocity structure in our ANT results, e.g., within the Bohemian Massif, beneath the Molasse basin, in the Southern Alps and generally in the easternmost profile *Dd*. This effect might be caused by a combination of two factors: (1) the crust and the uppermost mantle velocity structure east of longitude 12°E within the European and the Adria plate could be significantly different and more complex than further west, and (2) our depth inversions suffer from a degradation in data coverage with depth or from a non-optimal initial reference layering.

4. Conclusions

We have derived a new 3-D v_S model that fits surface wave group dispersion curves between 3 and 35 s. Our model explains data from the permanent and the EASI AlpArray complementary experiment broadband seismic stations, with a significant reduction of surface-wave data variance. The strength and quality of this new information relies on the absolute velocity and the velocity gradient being continuously and unambiguously sampled along the Moho, only limited by the amount, quality and back-azimuthal distribution of the data available.

Our preferred model consists of 3 crustal layers (sediment, upper and lower crust) with the shear velocity described by a linear gradient. The final 3D model (i) is a complete model that include the isotropic elastic parameters (v_P, v_S and density), (ii) can be considered an improvement of existing reference models like EPcrust (Molinari and Morelli, 2011), which has the same vertical parametrization, (iii) incorporates a priori information of recent progress in terms of crustal structure from independent methods (Spada et al., 2013; Molinari and Morelli, 2011) and (iv) is, in principle, suited for many applications such as wave propagation modelling, crustal correction, gravity studies, etc..

Despite the fact that during the time of writing, a new and dense dataset has been made available – the AlpArray seismic network data (Hetényi et al., 2018c)–, and recent models have been published (Lu et al., 2020; Qorbani et al., 2020; Magrin and Rossi, 2020), we believe that our study yields valuable results in terms of the 3D structure of the Eastern Alpine region. In particular, we found: (a) high correlation with the well-known geological features up to 20 km depth; (b) we image the inner structure of the Molasse basin; (c) we found important variations of crustal thickness and velocities as a result of Alpine orogeny.

The relatively poor ray coverage in the Eastern part and the strong 3D variability of the orogenic structure suggest that the inclusion of the new high-resolution dataset from the AlpArray Seismic Network will help to improve the resolution, coverage and the model details. Moreover, the derivation of nine-component cross-correlation functions to extract Love wave signals, combined with the measurements of both group and Love velocities would allow an increase of the resolution (horizontal and on depth) and a further investigation of the anisotropy in the crust.

Data availability

Waveform data from permanent network stations and from the EASI AlpArray complementary experiment stations are available through EIDA (http://www.orfeus-eu. org/eida/).

The permanent and temporary stations are contributed via the following networks codes: BW, CH (Swiss Seismological Service (SED) at ETH Zurich, 1983), CR, CZ (Institute of Geophysics, Academy of Sciences of the Czech Republic, 1973), HU, GE (GEOFON Data Centre, 1993), GR, HU (Kövesligethy Radó Seismological Observatory, 1992), IU (Albuquerque Seismological Laboratory (ASL)/USGS, 1988), IV (INGV Seismological Data Centre, 1997), MN (MedNet project partner institutions, 1988), NI (OGS (Istituto Nazionale di Oceanografia e di Geofisica Sperimentale) and University of Trieste, 2002), OE, OX (OGS (Istituto Nazionale di Oceanografia e di Geofisica Sperimentale), 2016), PL, SI, SK, SL, ST (Geological Survey-Provincia Autonoma di Trento, 1981), SX, TH, XT (AlpArray Seismic Network 2014).

Declaration of Competing Interest

The authors declare that they have no known competing financial interests or personal relationships that could have appeared to influence the work reported in this paper.

Acknowledgement

The authors acknowledge the AlpArray Working Group (http://www.alparray.ethz.ch) for making the AlpArray initiative possible. AlpArray Switzerland is funded by the Swiss-AlpArray SINERGIA project CRSII2_154434/1 by Swiss National Science Foundation (SNSF). GH acknowledges the support of the SNSF for project OROG3NY (grant PP00P2_157627). Full funding details for project EASI are found in Hetényi et al. (2018b). Figures have been prepared using the Generic Mapping tools (Wessel and Smith, 1998), Obspy (Krischer et al., 2015) and are made using perceptually uniform colormaps (Crameri, 2018). For careful reviews that greatly helped to improve the manuscript, we thank Giuliana Rossi and an anonymous reviewer.

The authors thanks the group of field operators, the *AlpArray-EASI Team:* Jaroslava Plomerová, Helena Munzarová, Ludek Vecsey, Petr Jedlicka, Josef Kotek, Götz Bokelmann, Irene Bianchi, Maria-Theresia Apoloner, Florian Fuchs, Patrick Ott, Ehsan Qorbani, Katalin Gribovszki, Peter Kolinsky, Peter Jordakiev, Hans Huber, Stefano Solarino, Aladino Govoni, Simone Salimbeni, Lucia Margheriti, Adriano Cavaliere, Edi Kissling, John Clinton, Roman Racine, Sacha Barman, Robert Tanner, Pascal Graf, Laura Ermert, Anne Obermann, Stefan Hiemer, Meysam Rezaeifar, Edith Korger, Ludwig Auer, Korbinian Sager, György Hetényi,

Irene Molinari, Marcus Herrmann, Saulé Zukauskaité, Paula Koelemeijer, Sascha Winterberg.

Author contribution

IM and AO performed data preparation and data analysis. IM performed the inversions and prepared the first manuscript. LB provided the tomography code used in the analysis. IM, EK and GH performed the geological interpretations of the result. GH coordinated the EASI complementary experiment and EK coordinated the AlpArray initiative. All authors contributed to reviewing and editing the manuscript.

Supplementary materials

Supplementary material associated with this article can be found, in the online version, at doi:10.1016/j.ringps.2020.100006.

References

Albuquerque Seismological Laboratory (ASL)/USGS, 1988. Global Seismograph Network (GSN – IRIS/USGS). International Federation of Digital Seismograph Networks, Other/Seismic Network doi:10.7914/SN/IU.

AlpArray Seismic Network, 2014. Eastern Alpine Seismic Investigation (EASI) - AlpArray Complimentary Experiment. AlpArray Working Group. Other/Seismic Network doi:10.12686/alparray/xt_2014.

Anselmi, M., Govoni, A., De Gori, P., Chiarabba, C., 2011. Seismicity and velocity structures along the south-Alpine thrust front of the Venetian Alps (NE-Italy). Tectonophysics 513, 1–4. doi:10.1016/j.tecto.2011.09.023, 37-48.

Babuška, V., Plomerová, J., 2013. Boundaries of mantle-lithosphere domains in the Bohemian Massif as extinct exhumation channels for high-pressure rocks. Gondwana Res. 23, 973–987. doi:10.1016/j.gr.2012.07.005.

Baran, R., Friedrich, A.M., Schlunegger, F., 2014. The late Miocene to Holocene erosion pattern of the Alpine foreland basin reflects Eurasian slab unloading beneath the western Alps rather than global climate change. Lithosphere 6 (2), 124–131. doi:10.1130/L307.1.

Barruol, G., Deschamps, A., Coutant, O., 2004. Mapping Upper mantle anisotropy beneath SE France by SKS splitting: evidence for a Neogene asthenospheric flow induced by the Apulian slab rollback and deflected by the deep Alpine roots. Tectonophysics 394, 125–138.

Behm, M., 2009. 3-D modelling of the crustal S-wave velocity structure from active source data: application to the Eastern Alps and the Bohemian Massif. Geophys. J. Int. 179 (1), 265–278. doi:10.1111/j.1365-246X.2009.04259.x.

Behm, M., Brückl, E., Chwatal, W., Thybo, H., 2007. Application of stacking and inversion techniques to three-dimensional wide- angle reflection and refraction seismic data of the Eastern Alps. Geophys. J. Int. 170 (1), 275–298.

Bianchi, I., Bokelmann, G., 2014. Seismic signature of the Alpine indentation, evidence from the Eastern Alps. J. Geodyn. 82, 69–77. doi:10.1016/j.jog.2014.07.005.

Bianchi, I., Miller, M.S., Bokelmann, G., 2014. Insights on the upper mantle beneath the Eastern Alps. Earth Planet. Sci. Lett. 403, 199–209. doi:10.1016/j.epsl.2014.06.051.

Bianchi, I., Behm, M., Rumpfhuber, E.M., Bokelmann, G., 2015. A new seismic data set on the depth of the Moho in the Alps. Pure Appl. Geophys. 172, 295–308. doi:10.1007/s00024-014-0953-1.

Bigi, G., Cosentino, D., Parotto, M., Sartori, R., Scandone, P., 1990. Structural model of Italy, 1:500.000. Quaderni de La Ricerca Scientifica. C.N.R. 114 (3).

Blundell, D., Freeman, R., Mueller, S. (Eds.), 1992. A Continent Revealed: The European Geotraverse, Structure and Dynamic Evolution. Cambridge University Press, Cambridge doi:10.1017/CBO9780511160826.

Bokelmann, G., Qorbani, E., Bianchi, I., 2013. Seismic anisotropy and large-scale deformation of the Eastern Alps. Earth Planet. Sci. Lett. 383, 1–6. doi:10.1016/j.epsl.2013.09.019.

Boschi, L., Dziewonski, A.M., 1999. High- and low-resolution images of the Earth's mantle: implications of different approaches to tomographic modelling. J. Geophys. Res. 104 (B11), 567–594 25.

Boschi, L., Weemstra, C., 2015. Stationary-phase integrals in the cross correlation of ambient noise. Rev. Geophys. 53, 411–451. doi:10.1002/2014RG000455.

Bousquet, R., Schmid , S.M., Zeilinger, G., Oberhänsli, R., Rosenberg, C., Molli, G., Robert, Ch., Wiederkehr, M., Rossi, Ph., 2012. Tectonic framework of the Alps. CCGM/CGMW.

Brenguier, F., Shapiro, N.M., Campillo, M., Nercessian, A., Ferrazzini, V., 2007. 3-D surface wave tomography of the Piton de la Fournaise volcano using seismic noise correlations. Geophys. Res. Lett. 34, L02305. doi:10.1029/2006GL028586.

Bressan, G., Gentile, G.F., Tondi, R., de Franco, R., Urban, S., 2012. Sequential integrated inversion of tomographic images and gravity data: an application to the Friuli area (North-Eastern Italy). Boll. Geof. Teor. Appl. 53, 191–212. doi:10.4430/bgta0059.

Brückl, E., Bodoky, T., Hegedüs, E., Hrubcová, P., Gosar, A., Grad, M., Guterch, A., Hajnal, Z., Keller, G.R., Špičák, A., Sumanovac, F., Thybo, H., Weber, F.ALP 2002 Working Group, 2003. ALP 2002 seismic experiment. Stud. Geophys. Geod. 47, 671–679. doi:10.1023/A:1024780022139.

Brückl, E., Bleibinhaus, F., Gosar, A., Grad, M., Guterch, A., Hrubcová, P., Keller, G.R., Majdański, M., Šumanovac, F., Tiira, T., Yliniemi, J., Hegedüs, E., Thybo, H., 2007. Crustal structure due to collisional and escape tectonics in the Eastern Alps region based on profiles Alp01 and Alp02 from the ALP 2002 seismic experiment. J. Geophys. Res. 112, B06308. doi:10.1029/2006JB004687.

Brückl, E., Behm, M., Decker, K., Grad, M., Guterch, A., Keller, G.R., Thybo, H., 2010. Crustal structure and active tectonics in the Eastern Alps. Tectonics 29, TC2011. doi:10.1029/2009TC002491.

Chiarabba, C., Jovane, L., Di Stefano, R., 2005. A New view of Italian seismicity using 20 years of instrumental recordings. Tectonophysics 395 (3), 251–268.

Crameri, F., 2018. Scientific colour-maps. Zenodo doi:10.5281/zenodo.1243862.

Di Stefano, R., Kissling, E., Chiarabba, C., Amato, A., Giardini, D., 2009. Shallow subduction beneath Italy: three-dimensional images of the Adriatic-European-Tyrrhenian lithosphere system based on high-quality P wave arrival times. J. Geophys. Res. 114, B05305. doi:10.1029/2008JB005641.

Di Stefano, R., Ciaccio, M.G., 2014. The lithosphere and asthenosphere system in Italy as inferred from the Vp and Vs 3D velocity model and Moho map. J. Geodyn. 82, 16–25.

Diehl, T., Husen, S., Kissling, E., Deichmann, N., 2009. High-resolution 3-D P-wave model of the Alpine crust. Geophys. J. Int. 179 (2), 1133–1147. doi:10.1111/j.1365-246X.2009.04331.x.

Doglioni, C., Bosellini, A., 1987. Eoalpine and Mesoalpine tectonics in the Southern Alps. Geol. Rundschau 76, 735–754.

Dziewonski, A.M., Anderson, D.L., 1981. Preliminary reference Earth model. Phys. Earth Planet. Inter. 25 (4), 297–356.

Faccenna, C., Becker, T.W., Lucente, F.P., Jolivet, L., Rossetti, F., 2001. History of subduction and back-arc extension in the Central Mediterranean. Geophys. J. Int. 145, 809–820. doi:10.1046/j.0956-540x.2001.01435.x.

Faccenna, C., Piromallo, C., Crespo-Blanc, A., Jolivet, L., Rossetti, F., 2004. Lateral slab deformation and the origin of the western Mediterranean arcs. Tectonics 23, TC1012. doi:10.1029/2002TC001488.

Faccenna, C., Becker, T., 2010. Shaping mobile belts by small-scale convection. Nature 465, 602–605. doi:10.1038/nature09064.

Froitzheim, N., Schmid, S.M., Frey, M., 1996. Mesozoic paleogeography and the timing of eclogitefacies metamorphism in the Alps: a working hypothesis. Eclogae Geologicae Helvetiae 89 (1), 81.

Fuchs, F., Kolínský, P., Gröschl, G., Bokelmann, G.the AlpArray Working Group, 2016. AlpArray in Austria and Slovakia: technical realization, site description and noise characterization. Adv. Geosci. 43, 1–13. doi:10.5194/adgeo-43-1-2016.

Geissler, W.H., Kampf, H., Skacelova, Z., Plomerova, J., Babuska, V., Kind, R., 2012. Lithosphere structure of the NE Bohemian Massif (Sudetes) - A teleseismic receiver function study. Tectonophysics 564-565, 12–37.

GEOFON Data Centre, 1993. GEOFON Seismic Network. Deutsches GeoForschungsZentrum GFZ doi:10.14470/TR560404.

Geological Survey-Provincia Autonoma di Trento, 1981. Trentino Seismic Network. International Federation of Digital Seismograph Networks, Other/Seismic Network doi:10.7914/SN/ST.

Govoni, A., Bonatto, L., Capello, M., Cavaliere, A., Chiarabba, C., D'Alema, E., Danesi, S., Lovati, S., Margheriti, L., Massa, M., Mazza, S., Mazzarini, F., Monna, S., Moretti, M., Nardi, A., Piccinini, D., Piromallo, C., Pondrelli, S., Salimbeni, S., Serpelloni, E., Solarino, S., Vallocchia, M., Santulin, M.the AlpArray Working Group, 2017. AlpArray-Italy: site description and noise characterization. Adv. Geosci. 43, 39–52. doi:10.5194/adgeo-43-39-2017.

Grászer, Z., Szanyi, G., Bondár, I., Czanik, C., Czifra, T., Győri, E., Hetényi, G., Kovács, I., Molinari, I., Süle, B., Szűcs, E., Wesztergom, V., Wéber, Z.AlpArray Working Group, 2018. AlpArray in Hungary: temporary and permanent seismological networks in the transition zone between the Eastern Alps and the Pannonian basin. Acta Geod. Geophys. 1–25. doi:10.1007/s40328-018-0213-4.

Grad, M., Tiira, T.ESC Working Groups, 2009. The Moho depth map of the European Plate. Geophys. J. Int. 176, 279–292.

Gualtieri, L., Serretti, P., Morelli, A., 2014. Finite-difference P-wave travel time seismic tomography of the crust and uppermost mantle in the Italian region. Geochem. Geophys. Geosyst. 15, 69–88. doi:10.1002/2013GC004988.

Guidarelli, M., Aoudia, A., Costa, G., 2017. 3-D structure of the crust and uppermost mantle at the junction between the Southeastern Alps and External Dinarides from ambient noise tomography. Geophys. J. Int. 211 (3), 1509–1523. doi:10.1093/gji/ggx379.

Guterch, A., Grad, M., Thybo, H., Keller, G.R., 1999. POLONAISE '97 – an international seismic experiment between Precambrian and Variscan Europe in Poland. Tectonophysics 314 (1–3), 101–121.

Guterch, A., Grad, M., Keller, G.R., Posgay, K., Vozár, J., Špičák, A., Brückl, E., Hajnal, Z., Thybo, H., Selvi, O.CELEBRATION 2000 Experiment Team, 2003. CELEBRATION 2000 seismic experiment. Stud. Geophys. Geod. 47 (3), 659–669.

Handy, M.R., Schmid, S.M., Bousquet, R., Kissling, E., Bernoulli, D., 2010. Reconciling plate-tectonic reconstructions with the geological-geophysical record of spreading and subduction in the Alps. Earth Sci. Rev. 102, 121–158.

Handy, M.R., Ustaszewski, K., Kissling, E., 2015. Reconstructing the Alps–Carpathians–Dinarides as a key to understanding switches in subduction polarity, slab gaps and surface motion. Int. J. Earth Sci. (Geol. Rundsch.) 104, 1–26. doi:10.1007/s00531-014-1060-3.

Hetényi, G., Ren, Y., Dando, B., Stuart, G.W., Hegedűs, E., Kovács, A.C., Houseman, G.A., 2015. Crustal structure of the Pannonian Basin: the AlCaPa and Tisza Terrains and the Mid-Hungarian Zone. Tectonophysics 646, 106–116. doi:10.1016/j.tecto.2015.02.004.

Hetényi, G., Epard, J.L., Colavitti, L., Hirzel, A.H., Kiss, D., Petri, B., Scarponi, M., Schmalholz, S.M., Subedi, S., 2018a. Spatial relation of surface faults and crustal seismicity: a first comparison in the region of Switzerland. Acta Geod. Geophys. 53, 439–461. doi:10.1007/s40328-018-0229-9.

Hetényi, G., Plomerová, J., Bianchi, I., Kampfová Exnerová, H., Bokelmann, G., Handy, M.R., Babuška, V., 2018b. From mountain summits to roots: crustal structure of the Eastern Alps and Bohemian Massif along longitude 13.3° E. Tectonophysics 744, 239–255. doi:10.1016/j.tecto.2018.07.001.

Hetényi, G., Molinari, I., Clinton, J., Bokelmann, G., Bondár, I., Crawford, W.C., Dessa, J.X., Doubre, C., Friederich, W., Fuchs, F., Giardini, D., Gráczer, Z., Handy, M.R., Herak, M., Jia, Y., Kissling, E., Kopp, H., Korn, M., Margheriti, L., Meier, T., Mucciarelli, M., Paul, A., Pesaresi, D., Piromallo, C., Plenefisch, T., Plomerová, J., Ritter, J., Rümpker, G., Šipka, V., Spallarossa, D., Thomas, C., Tilmann, F., Wassermann, J., Weber, M., Wéber, Z., Wesztergom, V., Živčić, M.AlpArray Seismic Network Team, AlpArray OBS Cruise Crew, the AlpArray Working Group, 2018c. The AlpArray Seismic Network – a large-scale European experiment to image the Alpine orogen. Surv. Geophys. 39, 1009–1033. doi:10.1007/s10712-018-9472-4.

Hinsch, R., 2013. Laterally varying structure and kinematics of the Molasse fold and thrust belt of the Central Eastern Alps: implications for exploration. Am. Assoc. Pet. Geol. Bull. 97 (10), 1805–1831. doi:10.1306/04081312129.

Horváth, F., Bada, G., Szafián, P., Tari, G., Ádám, A., Cloetingh, S., 2006. Formation and deformation of the Pannonian Basin: constraints from observational data. In: European Lithosphere Dynamics, 32. Geological Society of London Memoirs, Geological Society of London, pp. 191–206 eds Gee, D. & Stephensen, R.,.

Horváth, F., Musitz, B., Balázs, A., Végh, A., Uhrin, A., Nádor, A., Koroknai, B., Pap, N., Tóth, T., Wórum, G., 2015. Evolution of the Pannonian basin and its geothermal resources. Geothermics 53, 328–352. doi:10.1016/j.geothermics.2014.07.009.

Hrubcová, P., Środa, P., Špičák, A., Guterch, A., Grad, M., Keller, G.R., Brueckl, E., Thybo, H., 2005. Crustal and uppermost mantle structure of the Bohemian Massif based on CELEBRATION 2000 data. J. Geophys. Res. 110, B11305. doi:10.1029/2004JB003080.

Hrubcová, P., Środa, P., 2008. Crustal structure at the easternmost termination of the Variscan belt based on CELEBRATION 2000 and ALP 2002 data. Tectonophysics 460 (1—4), 55–75.

Hrubcová, P., Geissler, W.H., 2009. The crust-mantle transition and the Moho beneath the Vogtland/West Bohemian region in the light of different seismic methods. Stud. Geophys. Geod. 53, 275–294. doi:10.1007/s11200-009-0018-6.

Hrubcová, P., Środa, P., Grad, M., Geissler, W.H., Guterch, A., Vozár, J., Hegedűs, E., 2010. From the Variscan to the Alpine Orogeny: crustal structure of the Bohemian Massif and the Western Carpathians in the light of the SUDETES 2003 seismic data. Geophys. J. Int. 183 (2), 611–633. doi:10.1111/j.1365-246X.2010.04766.x.

Husen, S., Diehl, T., Kissling, E., 2009. The effects of data quality in local earthquake tomography: application to the Alpine region. Geophysics 74 (6), WCB71–WCB79.

INGV Seismological Data Centre, 1997. Rete Sismica Nazionale (RSN). Istituto Nazionale di Geofisica e Vulcanologia (INGV), Italy doi:10.13127/SD/X0FXnH7QfY.

Institute of Geophysics, Academy of Sciences of the Czech Republic, 1973. Czech Regional Seismic Network. International Federation of Digital Seismograph Networks, Other/Seismic Network doi:10.7914/SN/CZ.

Jolivet, L., Faccenna, C., Piromallo, C., 2009. From mantle to crust: stretching the Mediterranean. Earth Planet. Sci. Lett. 285, 1–2. doi:10.1016/j.epsl.2009.06.017, 198-209.

Karousová, H., Plomerová, J., Babuška, V., 2012. Three-dimensional velocity model of the crust of the Bohemian Massif and its effects on seismic tomography of the upper mantle. Stud. Geophys. Geod. 56, 249–267. doi:10.1007/s11200-010-0065-z.

Karousová, H., Plomerová, J., Babuška, V., 2013. Upper mantle structure beneath the southern Bohemian Massif and its surroundings imaged by high-resolution tomography. Geophys. J. Int. 194, 1203–1215. doi:10.1093/gji/ggt159.

Kästle, E.D., El-Sharkawy, A., Boschi, L., Meier, T., Rosenberg, C., Bellahsen, N., Cristiano, L., Weidle, C., 2018. Surface wave tomography of the Alps using ambient-noise and earthquake phase velocity measurements. J. Geophys. Res: Solid Earth 123 (2), 1770–1792.

Kästle, E.D., Rosenberg, C., Boschi, L., Bellahsen, N., Meier, T., El-Sharkawy, A., 2020. Slab break-offs in the Alpine subduction zone. Int. J. Earth Sci. (Geol. Rundsch.) 109, 587–603. doi:10.1007/s00531-020-01821-z.

Kissling, E., Schmid, S.M., Lippitsch, R., Ansorge, J., Fügenschuh, B., 2006. Lithosphere structure and tectonic evolution of the Alpine arc: new evidence from high-resolution teleseismic tomography. In: European Lithosphere Dynamics. Geological Society, London, pp. 129–145 eds Gee, D.G. & Stephenson, R.A.Memoirs 32.

Kissling, E., Schlunegger, F., 2018. Rollback orogeny model for the evolution of the Swiss Alps. Tectonics 37, 1097–1115. doi:10.1002/2017TC004762.

Krischer, L., Megies, T., Barsch, R., Beyreuther, M., Lecocq, T., Caudron, C., Wassermann, J., 2015. ObsPy: a bridge for seismology into the scientific Python ecosystem. Comput. Sci. Discov. 8, 014 003. doi:10.1088/1749-4699/8/1/014003.

Kövesligethy Radó Seismological Observatory (Geodetic and Geo- physical Institute, R. C. for A. and E. S., Hungarian Academy of Sciences (MTA CSFK GGI KRSZO)), 1992. Hungarian National Seismological Network. Deutsches GeoForschungsZentrum GFZ doi:10.14470/UH028726.

Kummerow, J., Kind, R., Oncken, O., Giese, P., Ryberg, T., Wylegalla, K., Scherbaum, F., 2004. A natural and controlled source seismic profile through the Eastern Alps: TRANSALP. Earth Planet. Sci. Lett. 225, 115–129. doi:10.1016/j.epsl.2004.05.040.

Lebedev, S., Adam, J.M.-C., Meier, T., 2013. Mapping the Moho with seismic surface waves: a review, resolution analysis, and recommended inversion strategies. Tectonophysics 609, 377–394.

Lippitsch, R., Kissling, E., Ansorge, J., 2003. Upper mantle structure beneath the Alpine orogen from high-resolution teleseismic tomography. J. Geophys. Res. 108, 2376. doi:10.1029/2002JB002016, B8.

Lu, Y., Stehly, L., Paul, A.the AlpArray Working Group, 2018. High-resolution surface wave tomography of the European crust and uppermost mantle from ambient seismic noise. Geophys. J. Int. 214 (2), 1136–1150.

Lu, Y., Stehly, L., Brossier, L., Paul, A.the AlpArray Working Group, 2020. Imaging Alpine crust using ambient noise wave-equation tomography. Geophys. J. Int. 222 (1), 69–85. doi:10.1093/gji/ggaa145.

Magrin, A., Rossi, G., 2020. Deriving a New Crustal Model of Northern Adria: the Northern Adria Crust (NAC) Model. Front. Earth Sci. 8, 89. doi:10.3389/feart.2020.00089.

Matte, Ph., Maluski, H., Rajlich, P., Franke, W., 1990. Terrane boundaries in the Bohemian Massif: results of large-scale Variscan shearing. Tectonophysics 177, 151–170.

MedNet project partner institutions, 1988. Mediterranean Very Broadband Seismographic Network (MedNet). Istituto Nazionale di Geofisica e Vulcanologia (INGV), Italy, doi:10.13127/SD/fBBBtDtd6q.

Michelini, A., Živčić, M., Suhadolc, P., 1998. Simultaneous inversion for velocity structure and hypocenters in Slovenia. J. Seismol. 2, 257–265. doi:10.1023/A:1009723017040.

Mitterbauer, U., Behm, M., Brückl, E., Lippitsch, R., Guterch, A., Keller, G.R., Koslovskaya, E., Rumpfhuber, E.M., Sumanovac, F., 2011. Shape and origin of the East-Alp slab constrained by the ALPASS teleseismic model. Tectonophysics 510, 195–206.

Mlčoch, B., Konopásek, J., 2010. Pre-late Carboniferous geology along the contact of the Saxothuringian and Teplá–Barrandian zones in the area covered by younger sediments and volcanics (western Bohemian Massif, Czech Republic). J. Geosci. 55, 81–94. doi:10.3190/jgeosci.068.

Molinari, I., Morelli, A., 2011. EPcrust: a reference crustal model for the European plate. Geophys. J. Int. 185 (1), 352–364. doi:10.1111/j.1365-246X.2011.04940.x.

Molinari, I., Argnani, A., Morelli, A., Basini, P., 2015a. Development and testing of a 3D seismic velocity model of the Po Plain sedimentary basin, Italy. Bull. Seismol. Soc. Am. 15 (2a). doi:10.1785/0120140204.

Molinari, I., Verbeke, J., Boschi, L., Kissling, E., Morelli, A., 2015b. Italian and Alpine three-dimensional crustal structure imaged by ambient-noise surface-wave dispersion. Geochem. Geophys. Geosyst. 16. doi:10.1002/2015GC006176.

Molinari, I., Clinton, J., Kissling, E., Hetényi, G., Giardini, D., Stipčević, J., Dasović, I., Herak, M., Šipka, V., Wéber, Z., Gráczer, Z., Solarino, S.the Swiss-AlpArray Field Team, the AlpArray Working Group, 2016. Swiss-AlpArray temporary broadband seismic stations deployment and noise characterization. Adv. Geosci. 43, 15–29. doi:10.5194/adgeo-43-15-2016.

Mordret, A., Rivet, D., Landès, M., Shapiro, N.M., 2015. 3-D shear-velocity anisotropic model of Piton de la Fournaise volcano (La Réunion Island) from ambient seismic noise. J. Geophys. Res.: Solid Earth 120 (1), 406–427. doi:10.1002/2014JB011654.

Müller, M., Nieberding, F., Wanninger, A., 1988. Tectonic style and pressure distribution at the northern margin of the Alps between Lake Constance and the River Inn. Geol. Rundschau 77, 787–796.

Obermann, A., Lupi, M., Mordret, A., Jakobsdóttir, S., Miller, S., 2016. 3D-ambient noise Rayleigh wave tomography of Snæfellsjökull volcano, Iceland. J. Volcanol. Geotherm. Res. 317, 42–52. doi:10.1016/j.jvolgeores.2016.02.013.

Obermann, A., Molinari, I., Métaxian, J.P., Grigoli, F., Strauch, W., Wiemer, S., 2019. Structure of Masaya and Momotombo volcano, Nicaragua, investigated with a temporary seismic network. J. Volcanol. Geotherm. Res. 379, 1–11.

OGS (Istituto Nazionale di Oceanografia e di Geofisica Sperimentale) and University of Trieste, 2002. North-East Italy Broadband Network, International Federation of Digital Seismograph Networks. Other/Seismic Network, doi:10.7914/SN/NI.

OGS (Istituto Nazionale di Oceanografia e di Geofisica Sperimentale), 2016 doi:10.7914/SN/OX.

Ortner, H., Aichholzer, S., Zerlauth, M., Pilser, R., Fügenschuh, B., 2015. Geometry, amount, and sequence of thrusting in the Subalpine Molasse of western Austria and southern German y. Eur. Alps. Tectonics 34, 1–30. doi:10.1002/2014TC003550.

Paige, C., Saunders, M., 1982. LSQR: an algorithm for sparse linear equations and sparse least squares. Trans. Math. Softw. 8 (1), 43–71.

Piromallo, C., Morelli, A., 2003. P wave tomography of the mantle under the Alpine-Mediterranean area. J. Geophys. Res. 108 (B2), 2065. doi:10.1029/2002JB001757.

Plomerová, J., Achauer, U., Babuška, V., Vecsey, L.BOHEMA Working Group, 2007. Upper mantle beneath the Eger Rift (Central Europe): plume or asthenosphere upwelling? Geophys. J. Int. 169 (2), 675–682. doi:10.1111/j.1365-246X.2007.03361.x.

Plomerová, J., Munzarová, H., Vecsey, L., Kissling, E., Achauer, U., Babuška, V., 2016. Cenozoic volcanismin the Bohemian Massif in the context of P- and S-velocity high-resolution teleseismic tomography of the upper mantle. Geochem. Geophys. Geosyst. 17, 3326–3349. doi:10.1002/2016GC006318.

Qorbani, E., Zigone, D., Handy, M.R., Bokelmann, G.the AlpArray-EASI working group, 2020. Crustal structures beneath the Eastern and Southern Alps from ambient noise tomography. Solid Earth Discuss. doi:10.5194/se-2019-177, In Review.

Ren, Y., Grecu, B., Stuart, G., Houseman, G., Hegedüs, E.South Carpathian Project Working Group, 2013. Crustal structure of the Carpathian-Pannonian region from ambient noise tomography. Geophys. J. Int. 195 (2), 1351–1369. doi:10.1093/gji/ggt316.

Ritzwoller, M.H., Levshin, A.L., 1998. Eurasian surface wave tomography: group velocities. J. Geophys. Res. 103 (B3), 4839–4878.

Rosenberg, C.L., Schneider, S., Scharf, A., Bertrand, A., Hammerschmidt, K., Rabaute, A., Brun, J.-.P., 2018. Relating collisional kinematics to exhumation processes in the Eastern Alps. Earth Sci. Rev. 176, 311–344. doi:10.1016/j.earscirev.2017.10.013.

Sambridge, M., 1999. Geophysical inversion with a Neighbourhood Algorithm-I. Searching a parameter space. Geophys. J. Int. 138 (2), 479–494.

Schaefer, J.F., Boschi L., Kissling E., 2011. Adaptively parametrized surface wave tomography: methodology and a new model of the European upper mantle. 186, 1431–1453, doi: 10.1111/j.1365-246X.2011.05135.x.

Scharf, A., Handy, M.R., Favaro, S., Schmid, S.M., Bertrand, A., 2013. Modes of orogen-parallel stretching and extensional exhumation in response to microplate indentation and rollback subduction (Tauern Window, Eastern Alps). Int. J. Earth Sci. (Geol. Rundsch.) 102, 1627–1654. doi:10.1007/s00531-013-0894-4, 1.

Schippkus, S., Zigone, D., Bokelmann, G.the AlpArray Working Group, 2018. Ambient-noise tomography of the wider Vienna Basin region. Geophys. J. Int. 215 (1), 102–117. doi:10.1093/gji/ggy259.

Schlunegger, F., Kissling, E., 2015. Slab rollback orogeny in the Alps and evolution of the Swiss Molasse basin. Nat. Commun. 6, 8605. doi:10.1038/ncomms9605.

Schmid, S.M., Bernoulli, D., Fügenschuh, B., Matenco, L., Schefer, S., Schuster, R., Tis-

chler, M., Ustaszewski, K., 2008. The Alpine-Carpathian-Dinaridic orogenic system: correlation and evolution of tectonic units. Swiss Journal of Geosciences 101 (1), 139–183.

Schmid, S.M., Scharf, A., Handy, M.R., Rosenberg, C.L., 2013. The Tauern Window (Eastern Alps, Austria): a new tectonic map, with cross-sections and a tectonometamorphic synthesis. Swiss J. Geosci. 106, 1–32. doi:10.1007/s00015-013-0123-y.

Serpelloni, E., Vannucci, G., Anderlini, L., Bennett, R., 2016. Kinematics, seismotectonics and seismic potential of the eastern sector of the European Alps from GPS and seismic deformation data. Tectonophysics 688, 157–181. doi:10.1016/j.tecto.2016.09.026.

Singer, J., Diehl, T., Husen, S., Kissling, E., Duretz, T., 2014. Alpine lithosphere slab rollback causing lower crustal seismicity in northern foreland. Earth Planet. Sci. Lett. 397, 42–56. doi:10.1016/j.epsl.2014.04.002.

Sommaruga, A., Eichenberger, U., Mariller, F., 2012. Seismic Atlas of the Swiss Molasse Basin. Beiträge zur Geologie der Schweiz—Geophysik (text and 24 enclosures). Federal Office of Topography Swisstopo.

Spada, M., Bianchi, I., Kissling, E., Piana Agostinetti, N., Wiemer, S., 2013. Combining controlled-source seismology and receiver function information to derive 3-D Moho topography for Italy. Geophys. J. Int. 194 (2), 1050–1068.

Spooner, C., Scheck-Wenderoth, M., Götze, H.-J., Ebbing, J., Hetényi, G.the AlpArray Working Group, 2019. Density distribution across the Alpine lithosphere constrained by 3-D gravity modelling and relation to seismicity and deformation. Solid Earth 10, 2073–2088. doi:10.5194/se-10-2073-2019.

Środa, Czuba, W., Grad, M., Guterch, A., Tokarski, A.K., Janik, T., Rauch, M., Keller, G.R., Hegedüs, E., Vazár, J.CELEBRATION 2000 Working Group, 2006. Crustal and upper mantle structure of the western Carpathians from CELEBRATION 2000 profiles CEL01 and CEL04: seismic models and geological implications. Geophys. J. Int. 167 (2), 737–760.

Stipčević, J., Herak, M., Molinari, I., Dasović, I., Tkalčić, H., Gosar, A., 2020. Crustal thickness beneath the Dinarides and surrounding areas from receiver functions. Tectonics 39. doi:10.1029/2019TC005872.

Šumanovac, F., Orešković, J., Grad, M.ALP 2002 Working Group, 2009. Crustal structure at the contact of the Dinarides and Pannonian basin based on 2-D seismic and gravity interpretation of the Alp07 profile in the ALP 2002 experiment. Geophys. J. Int. 179 (1), 615–633. doi:10.1111/j.1365-246X.2009.04288.x.

Swiss Seismological Service (SED) at ETH Zurich, 1983. National Seismic Networks of Switzerland. ETH Zürich doi:10.12686/sed/networks/ch.

Tesauro, M., Kaban, M.K., Cloetingh, S.A., 2008. EuCRUST-07: a new reference model for the European crust. Geophys. Res. Lett. 35, L05313. doi:10.1029/2007GL032244.

Vecsey, L., Plomerová, J., Jedlička, P., Munzarová, H., Babuška, V.the AlpArray working group, 2017. Data quality control and tools in passive seismic experiments exemplified on the Czech broadband seismic pool MOBNET in the AlpArray collaborative project. Geosci. Instrum. Method. Data Syst. 6, 505–521. doi:10.5194/gi-6-505-2017.

Viganò, A., Scafidi, D., Ranalli, G., Martin, S., Della Vedova, B., Spallarossa, D., 2015. Earthquake relocations, crustal rheology, and active deformation in the central–eastern Alps (N Italy). Tectonophysics 661, 81–98. doi:10.1016/j.tecto.2015.08.017.

Vilhelm, J., Ivankina, T., Lokajíček, T., Rudajev, V., 2016. Comparison of laboratory and field measurements of P and S wave velocities of a peridotite rock. Int. J. Rock Mech. Min. Sci. 88 (2016), 235–241.

Waldhauser, F., Kissling, E., Ansorge, J., Mueller, S., 1998. Three-dimensional interface modelling with two-dimensional seismic data: the Alpine crust-mantle boundary. Geophys. J. Int. 135, 264–278.

Wathelet, M., 2008. An improved neighborhood algorithm: parameter conditions and dynamic scaling. Geophys. Res. Lett. 35.

Wessel, P., Smith, W.H.F., 1998. New, improved version of the Generic Mapping Tools released. Eos Trans. AGU 79, 579.

Wilde-Piórko, M., Saul, J., Grad, M., 2005. Differences in the Crustal and Uppermost Mantle Structure of the Bohemian Massif from Teleseismic Receiver Functions. Stud. Geophys. Geod. 49, 85–107. doi:10.1007/s11200-005-1627-3.

Yao, H., van der Hilst, R.D., de Hoop, M.V., 2006. Surface-wave array tomography in SE Tibet from ambient seismic noise and two-station analysis: I - Phase velocity maps. Geophys. J. Int. 166 (2), 732–744. doi:10.1111/j.1365-246X.2006.03028.x.

Ye, S., Ansorge, J., Kissling, E., St, Mueller, 1995. Crustal structure beneath the eastern Swiss Alps derived from seismic refraction data. Tectonophysics 242, 3–4. doi:10.1016/0040-1951(94)00209-R, 199-221.

Zhao, L., Paul, A., Malusà, M.G., Xu, X., Zheng, T., Solarino, S., Guillot, S., Schwartz, S., Dumont, T., Salimbeni, S., Aubert, C., Pondrelli, S., Wang, Q., Zhu, R., 2016. Continuity of the Alpine slab unraveled by high-resolution P wave tomography. J. Geophys. Res.: Solid Earth 121 (12), 8720–8737. doi:10.1002/2016JB013310.